To the Graduate Counsil:

I am submitting herewith a thesis written by Stephen Bruce Fitch entitled "A Transmission Electron Microscopy Examination of Plessite Structures in the Arispe Iron Meteorite." I have examined the final copy of this thesis for form and content and recommend that it be accepted in partial fulfillment of the requirements for the degree of Master of Science, with a major in Metallurgical Engineering.

Charlie R. Brooks

Charlie Brooks, Major Professor

We have read this thesis and recommend its acceptance:

Lawrence A. Taylor

Accepted for the Council:

Associate Vice Chancellor and
Dean of The Graduate School

A Transmission Electron Microscopy Examination of Plessite Structures in the Arispe Iron Meteorite

A Thesis
Presented for the
Master of Science
Degree
The University of Tennessee, Knoxville

Stephen B. Fitch
December 1999

DEDICATION

This thesis is dedicated to my wife,

Jennifer

and our sons,

Franklin and Jack

for all their love, patience, and support.

ACKNOWLEDGMENTS

There have been many persons that I have met that have great influence on my presence here today. I must first mention Dr. Gabriel Carro who introduced me to Metallurgy, inspired me to earn my Master of Science and suggested I seek out Dr. Charles Brooks as my major professor. I am very grateful that I followed his advice and I wish to thank Dr. Brooks for his guidance and mentoring. I am also grateful for the participation of the other committee members, Drs. Anthony Pedraza and Lawrence Taylor. I wish to thank Dr. John Dunlap for his assistance.

I thank my employer, Technology for Energy Corporation, for the financial support. I wish to thank my co-workers for their assistance and support. I also thank Dr. Lawrence Allard with Oak Ridge National Laboratory for the use of Mactempas.

Finally, I wish to thank my wife, Jennifer, and our sons, Franklin and Jack. They have been very supportive, understanding and patient as I completed my course work and thesis.

Abstract

The Arispe iron meteorite contains thin stingers of retained austenite (taenite) between plates of ferrite (kamacite). These stringers contain microstructures of various Fe-Ni phases called plessite. Plessite has been observed in the Arispe iron meteorite as fine and coarsened pearlitic (lamellar), spheroiditic, and microwidmanstätten α structure. Each of these structures consists of kamacite and a high-Ni unidentified taenite phase. Identification of the high-Ni taenite phase can aid in the determination of the Fe-Ni phase diagram. Through TEM observations and EDS analyses of the pearlitic plessite, this high-Ni phase was determined to be tetrataenite, an ordered face-centered cubic phase with ~50% Ni. Furthermore, it was concluded that the pearlitic plessite formed by the monotectoid reaction which is prior to the transformation of the taenite to tetrataenite. The taenite phase of the microwidmanstätten α structure was found to contain ~30% Ni, which is significantly less than the Ni content of tetrataenite. It is speculated that the microwidmanstätten α structure formed by a different mechanism. Based upon the observation of martensite in the microwidmanstätten α structure, the plessite formed from a stringer that was martensitic prior to transforming to microwidmanstätten α structure. It was not established why the taenite plates did not transform to a taenite phase as predicted from the Fe-Ni phase diagram.

TABLE OF CONTENTS

CHAPTER		PAGE
I.	INTRODUCTION	1
II	TERMINOLOGY AND DEFINITIONS	2
	Types of Meteorites	2
	Classification of Meteorites	2
	Structural Classification	2
	Chemical Classification	3
	Major Phases, Structures and Inclusions of Meteorites	4
III.	ORIGINS OF IRON METEORITES	7
IV	LITERATURE SURVEY	10
	Benefits / Significance of Meteorite Studies	10
	The Fe-Ni Phase Diagram	10
	Cooling Rates	13
	Plessite	13
V.	BACKGROUND OF THE ARISPE IRON METEORITE	19
VI.	EXPERIMENTAL PROCEDURES	21
VII.	RESULTS	29
VIII.	DISCUSSION	61
IX.	CONCLUSIONS AND RECOMMENDATIONS	70
	REFERENCES	71
	VITA	74

LIST OF FIGURES

FIGURE PAGE

1. Cooling Rates....9
2. Models of Parent Bodies of the Iron Meteorites....9
3. The Fe-Ni Phase Diagram....11
4. Taenite Grain....14
5. The M-Profile....14
6. Formation of the M-Profile....15
7. Schematic drawing of the zoned taenite....17
8. SEM Image of OTR and CZ....17
9. The Arispe Meteorite....20
10. Schematic View of the M-Profile of the Arispe Meteorite....20
11. TEM Sample of Microwidmanstätten α Structure....22
12. An example of the EDS spectra obtained....24
13. Cubic Structure of Tetrataenite....26
14. Tetrataenite crystal oriented to a [110] zone axis....27
15. Tetrataenite crystal oriented to a [101] zone axis....28
16. SEM image of Pearlitic Plessite from Sample A....31
17. SEM image of Area A in Figure 16....31
18. TEM Observation of γ Plates....32
19. SEM image of γ plate and α from TEM Sample A....34
20. TEM observation of α....35
21. Diffraction Pattern of γ Plate from Sample A....36
22. Diffraction Pattern of γ Plate from Sample A....36
23. SEM Image of Pearlitic Plessite from Sample A....38
24. TEM Observation of γ Plate....39

25. TEM Observation of γ Plate....40
26. Coarsening Pearlitic Plessite from Sample A....41
27. SEM Images of Pearlitic Plessite....42
28. TEM Observation of γ Plate....43
29. TEM Observation of γ Plate....45
30. TEM Observation of γ Plate....46
31. TEM Observation of γ Plate....47
32. TEM Observation of γ Plate....48
33. SEM Image of Microwidmanstätten Structure in Sample C....49
34. TEM observation of Microwidmanstätten Structure....50
35. TEM observation of Microwidmanstätten Structure....52
36. TEM observation of Microwidmanstätten Structure....53
37. Microwidmanstätten Structure in Sample D....55
38. TEM Observation of Primary α....56
39. TEM Observation of Primary α....57
40. SEM Image of Microwidmanstätten Structure from Sample E....58
41. SEM Image of Electropolished Microwidmanstätten Structure from Sample F....60
42. SEM Image of Microwidmanstätten Structure from Sample F....60
43. Fe-Ni Phase Diagram....63
44. Schematic View of Plessite Microstructure Formation....64
45. The M-profile Formation of the Arispe Meteorite....65
46. Schematic View of Pearlitic Plessite Formation....67
47. Schematic View of Microwidmanstätten Structure....69

I. Introduction

The sight of a meteor streaking through the night sky has fascinated mankind for as long as history has been recorded. Meteorites have also been long since revered as gifts from the heavens, as if to possess some special knowledge. From a different point of view, this holds true today. Meteorites are mankind's best record of the solar system's birth and history. Through the studies of meteorites, theories and pictures of the meteorites' preterrestrial life can be drawn. The orbits they may have had, the collisions they had with each other, and where they came from are recorded in the features within the meteorites themselves.

The iron meteorites provide a unique source of data for the determination of the low temperature region of the Fe-Ni phase diagram. The microstructures of the Arispe meteorite are one such source of the data. The microstructures themselves are unique in that they contain different morphologies within the same grain. It is the intent of this study to determine the phases and structures in the Arispe meteorite in order to gain a better understanding of the Fe-Ni phase diagram and of the formation of the microstructures.

II. Terminology and Definitions

A. Types of Meteorites

The classification of meteorites aids in the understanding of where and how they originated. Unfortunately, meteorites vary in macrostructure, microstructure, and chemical composition. Furthermore, some meteorites simply can not be classified within the structural classification.

The most commonly used classification was developed by Mason (1), which he later revised in 1967 (2). This classification, which is still used today, consists of four major groups: chondrites, achondrites, stony irons, and irons. Chondrites contain millimeter-sized spheres of silicate, known as chondrules. Chondrites contain 19 - 35 weight percent iron. The achondites contain no chondrules, have about 14 weight percent iron, and resemble terrestrial rock. The stony irons consist of equal portions of silicate minerals in an iron-nickel metal. Lastly, the irons consist mostly of iron and nickel. Each group is further divided by their own unique characteristics. Only the iron meteorites will be discussed here (3).

B. Classification of Iron Meteorites

In order to comprehend the classification of iron meteorites, two terms must be briefly defined. In meteoritic terminology, kamacite is the α-Fe with a body-centered cubic structure and low Ni (<7.5% in solid solution) content. Face-centered cubic austenite, γ-Fe, with high Ni, > 25%, is called taenite.

1. Structural Classification

Two approaches to the classification of iron meteorites have been made. The first is based on the measurement of the kamacite bandwidth. This method, although not thorough, is still used today to provide a general description of the meteorite. The four structural groups of iron meteorites are the hexahedrites, octahedrites, ataxites, and anamalous (3). Table 1 lists the structural classification of iron meteorites. Wasson (4) has pointed out that a major weakness of the structural classification is that it is based upon a purely physical characteristic and not an innate trait which may organize the meteorites in a more insightful manner.

Table 1. Structural Classification of Iron Meteorites (3).

Structural Class	Symbol	Bandwidth, mm
Hexahedrite	H	-
Coarsest Octahedrite	Ogg	>3.3
Coarse Octahedrite	Og	1.3 - 3.3
Medium Octahedrite	Om	0.5 - 1.3
Fine Octahedrite	Of	0.2 - 0.5
Finest Octahedrite	Off	<0.2, continuous
Plessitic Octahedrite	Opl	<0.2, spindles
Ataxites	D	-
Anomalous	Anom	Various

Hexahedrites are comprised of a single kamacite grain, usually much larger than the meteorite. The nickel content is very low, less than 0.06 weight percent. They are known to contain inclusions and Neumann bands (mechanical twins).

The structural classification known as Octahedrites is further subdivided by the width of the kamacite in the taenite (austenite with >25% Ni in solid solution) crystals. The name octahedrite is derived from the octahedral pattern of the kamacite (5). The kamacite nucleates on the taenite octahedral {111} planes (4). The bandwidths are determined by nickel content and the cooling rate of the meteor.

Plessitic Octahedrite describes the meteorites which contain a plessitic matrix with kamacite spindles scattered in an octahedral arrangement. Plessite is defined in the next section (IIC). The anomalous class covers the meteorites that do not fit any specific classification.

2. Chemical Classification

The first attempt at classifying iron meteorites by chemical composition was done by Goldberg et al.(6). His intentions were to classify the different groups in order to make a distinction in origin in time and place among the iron meteorites. His grouping was according to the percentage of Ni vs Ga. Each group was further categorized by the Ge and Ir concentrations. Lovering et al. (7) designated 4 groups, labeled I through IV, in descending amounts of Ga and

Ge. Wasson and Kimberlin (8) subdivided the groups by the amounts of Ga and Ge within each group. This subdivision is noted by a letter A, B, C, D, or E after the Roman numeral for each group. Several meteorites were found that could be classified between each division. These are noted with both appropriate letters. The one requirement to form a group is that each must contain at least 5 meteorites. A result of the work on the chemical classification is the rough correlation between the chemical groups and the structural groups. Table 2 shows the chemical groups and the correlated structures. Other elements (Ni, Co, Cu, Cr, Mn, Zn, Pb) may be present but less than one percent.

C. Major Phases, Structures and Inclusions of Meteorites

Five significant structures of the iron meteorites will be discussed: kamacite, taenite, Widmanstätten structure, martensite and plessite.

Kamacite (α) is the name given to ferrite iron containing up to 7.5% nickel. It is body-centered cubic and was first recognized as iron in meteorites before it was known to be a component of steel. As previously stated, the bandwidth of kamacite is used to classify iron meteorites.

Within kamacite grains, Neumann bands can be observed. These bands are mechanical twins that formed as a result of a preterrestrial collision. They appear as plate-shaped lamallae with widths varying from 1μ in precipitate-rich kamacite to 10μ in pure kamacite.

Martensite (α_2) forms by a diffusionless process from nickel-rich austenite. It grows parallel to the {111} planes of the parent austenite crystal and it maintains the same chemical composition as the parent austenite crystal.

Austenite, containing more than 25% nickel, is referred to as taenite (γ) (3). The stability of taenite is influenced by pressure. High pressure adds to the stability of taenite. The influence of pressure on taenite aids in the speculations of the meteorites' origins, i.e. their parent bodies (4).

The Widmanstätten structure is formed by kamacite precipitating as plates or bands on

Table 2. Structural Classes and Their Corresponding Chemical Classes (3).

Structural Class	Chemical Class
H	IIA
Ogg	IIB
Og	I, IIIE
Om	IIIA, IIIB,IID
Of	IVA; IIIC
Off	IIID
Opl	IIC
D	IVB

the octahedral planes, i.e. the {111} planes, of the taenite. The growth is diffusion-controlled and is a slow process. The final structure is obtained when a sufficiently low temperature has been reached and diffusion has ceased. It is the width of these kamacite bands in the Widmanstätten structure that is measured to determine the meteorites' classification. The width of the kamacite bands are influenced by three factors: (i) the nickel concentration, (ii) the cooling rate of the meteorite (iii) the nucleation temperature (9).

Plessite is the term given to the mixture of residual taenite and kamacite. It is the last structure to form from the taenite after the long, slow cooling process experienced by meteorites. The formation of plessite can occur by four different processes and it can vary in structure. Plessite will be discussed in further detail in the Literature Survey.

Cohenite is an orthorhombic mineral, $(Fe,Ni,Co)_3C$. It is closely related to iron carbide, Fe_3C, found in steels. It appears as brilliantly white in the optical microscope. It is characteristic of the Group I meteorites but is not uncommon in other groups.

Another common mineral is schreibersite. It is a phosphide $(Fe,Ni)_3P$ that appears yellow in reflective light. Shreibertsite can be observed as large skeleton crystals or of a vermicular shape. The microscopic form of schreibersite is called rhabdite, and it is plate-shaped or prisimatic. Schreibersite and rhabdite are present in a variety of meteorites, but not all.

Troilite is the name for a sulfide mineral with FeS composition. The inclusions may contain other sulfide minerals as well. They may occur as shapeless nodules, bars, diamonds, or dumbbells.

III. Origins of Iron Meteorites

Meteorite is the term given to stone or metal chunks from extra-terrestrial sources that have fallen to Earth. Before falling to Earth, they are meteors; prior to their terrestrial life, these stone or metal chunks are called meteoroids. From the investigations of their chemistries and physical characteristics, macro- and microscopic, several theories have been proposed for their origins.

It is generally believed that meteoroids originated from the asteroids in the solar system. These asteroids can be either those located between Mars and Jupiter, called belt asteroids, or those whose orbits either cross or approach Earth's orbit. Exactly how the belt asteroids were set loose from the belt is still under debate. It is suspected that these asteroids are from the Kirkwood gaps (empty regions with in the asteroid belt). The Kirkwood gaps are due to the gravitational resonance between the asteroids and Jupiter. By comparing the surface properties of asteroids and meteorites, a correlation has been made showing that both share similar chemical composition based on spectral analysis (10).

Asteroids and meteorites are possibly the planetary fossils of a planet that experienced a cataclysmic event at some time in the history of the solar system (1). The chemical and physical characteristics, i.e., the cooling rate, of meteorites lend some insight into the make-up of the parent body that might have once existed.

In terms of the chemistries of iron meteorites, Goldstein and Short (9) made some assumptions about the parent body. The various clustering of the Ge-Ga weight percentages of different iron meteorites suggested the possibility of more than one parent body. The idea of multiple parent bodies is also supported by Wasson and Kimberlin (8), based upon a Ge-Ni correlation.

Goldstein and Short (9) also used the cooling rates of iron meteorites to postulate the make-up of the iron meteorites' parent bodies. Based on their values and those of others, Goldstein and Short (9) also suggested the possibility of more than one parent body. As seen in

Figure 1, there is a variation in the cooling rate of the iron meteorite groups. In conjunction with the cooling rates and the influence of pressure on the Widmanstätten structure, Goldstein and Short (9) stated that a parent body of iron meteorites must have been smaller than 300 km.

Based on the overall data, four basic models of the parent body of iron meteorites have been developed. It is now assumed that they originated from one body and not several as proposed by Goldstein and Short. Figure 2 shows the four models. The first model, based on a central core, is not possible due to large variations of the cooling rates within the same groups, as shown in Figure 1. The basis for the other three models is that of earlier speculations of a multi-core parent body, or the "raisin bread" model as coined by Goldstein and Short (9).

Wetherill (12) has suggested that the asteroids could never form a single parent body. He proposes two scenarios. By the first scenario, Jupiter prevented the asteroids from clustering to eventually form a new planet. This would have kept the asteroids at their present size. The other scenario is that the same forces that influenced the formation of Jupiter and possibly Saturn acted on the asteroids. These forces accelerated the early asteroids to a velocity whereupon they collided and fragmented to their current size.

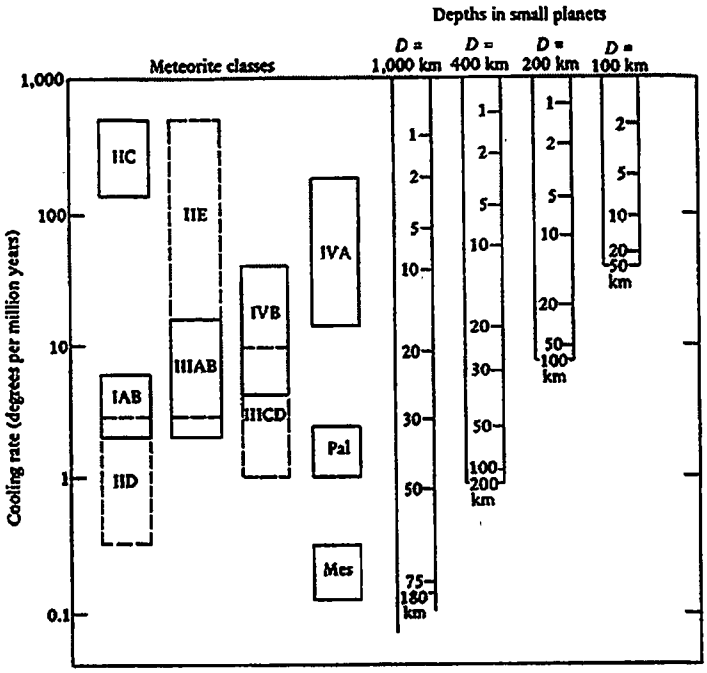


Figure 1 Cooling Rates (11).

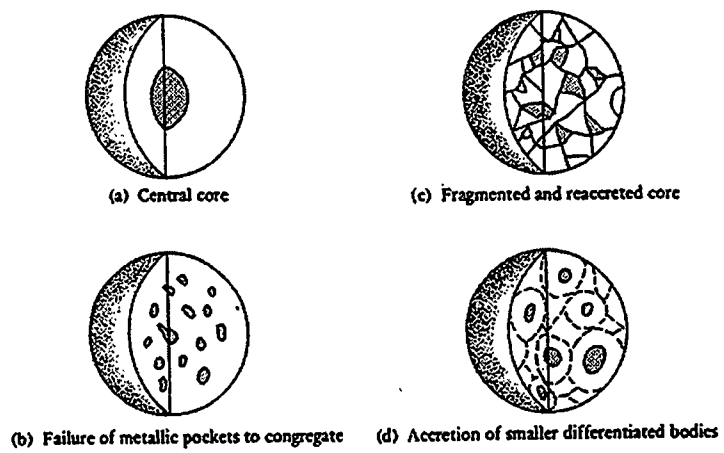


Figure 2 Models of Parent Bodies of the Iron Meteorites (11).

IV. Literature Survey

A. Benefits / Significance of Meteoritic Studies

From a metallurgical standpoint, the study of iron meteorites aids in the understanding of the Fe-Ni phase diagram. By analysis of the microstructure and microchemistry of the meteorites, the low temperature region of the Fe-Ni phase diagram can be determined. This is accomplished by the fact that meteorites cool at extremely slow rates (0.4-500°C / 10^6 years). At such low rates, the nickel atoms are given time to diffuse, and the system can reach equilibrium at low temperatures (<400°C). From the information obtained about the low temperature (<400°C) region of the Fe-Ni phase, the low temperature region of phase diagrams can be improved (13).

To a geologist, meteorites provide a record of the solar system. By compiling the chemical and structural characteristics, along with each meteorite's cooling rate, a model can be devised of the parent body or bodies that once existed at the formation of the solar system.

B. The Fe-Ni Phase Diagram

The iron-nickel phase diagram has been extensively studied (14-17). Most studies are in agreement on the high temperature region (>400°C). However, the low temperature (<400°C) region has been difficult to determine due to the sluggish movement of the atoms at that temperature. Due to their low cooling rate, iron meteorites contain the microstructures that develop from low temperature (<400°C) phase transformations.

The current phase diagram is shown in Figure 3 (17). Identification of the phases is shown in Table 3. Yang et al. (17) combined their study of plessite from six stony-iron meteorites, with the calculated phase diagram of Chuang et al. (14) and the diagram experimentally determined by Reuter et al. (15). Chuang et al.(14) considered the magnetic effect on the Gibb's free energy for their calculations. Reuter et al. (15) made revisions to the phase diagram through the analysis of microstructures within meteorites.

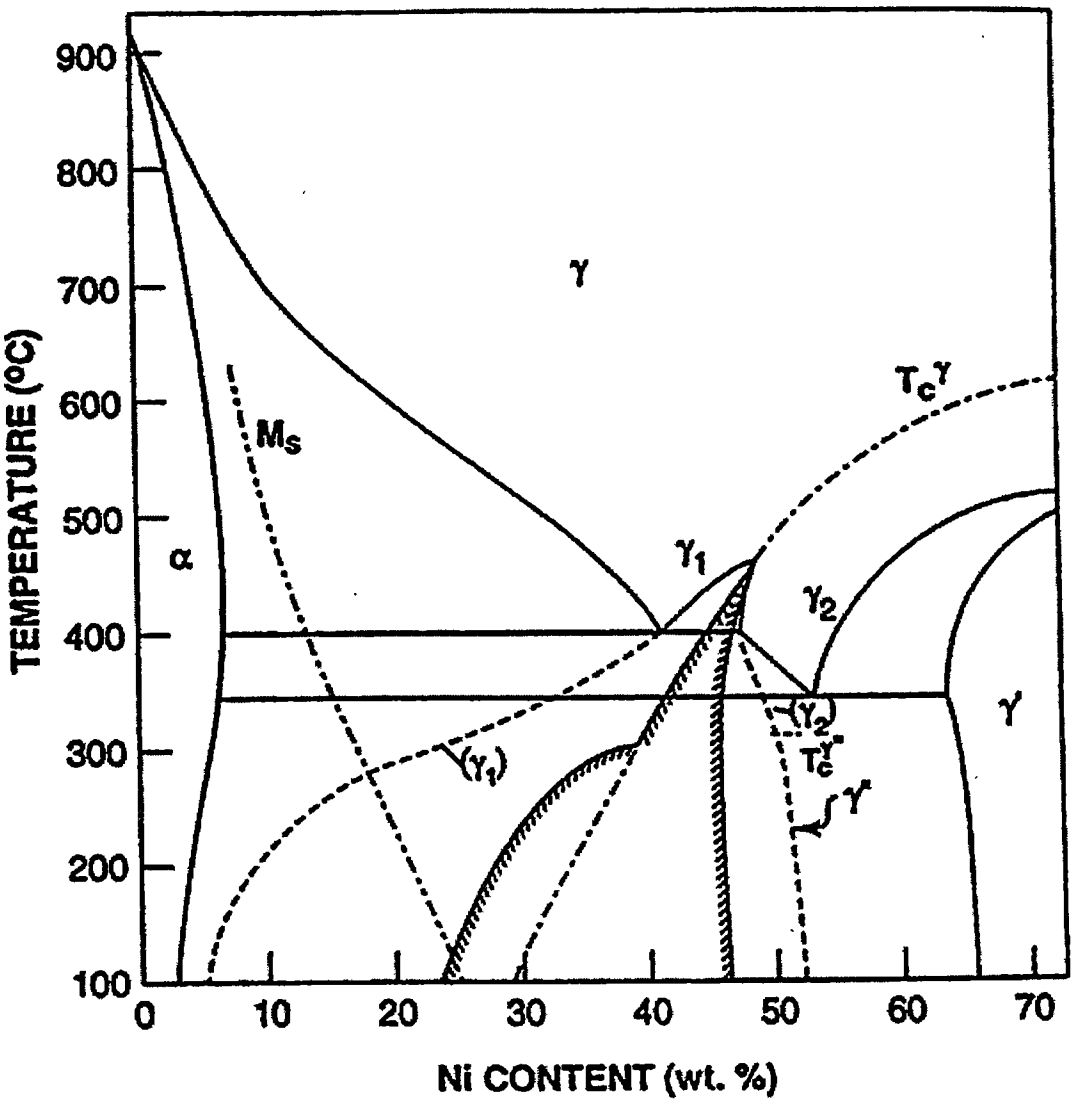


Figure 3 The Fe-Ni Phase Diagram (17).

Table 3. Identification of Phase on the Fe-Ni phase Diagram (17).

Symbol	Nomenclature	Phase
α	kamacite	low-Ni bcc
γ	taenite	high-temperature fcc
γ_1	-	low-Ni paramagnetic fcc
γ_2	-	high-Ni ferromagnetic
γ'	-	ordered Ni_3Fe
γ''	tetrataenite	ordered FeNi

The boundaries for the phases above 400°C were left unchanged from previous phase diagrams. Also, the tricritical point at 462°C and 48.8 wt. % Ni calculated by Chuang et al. (14) remained unchanged. Yang et al. (17) suggested some revisions. One is the incorporation of a monotectoid reaction ($\gamma_1 \rightarrow \alpha + \gamma_2$) at ~400°C along with eutectoid reaction ($\gamma_2 \rightarrow \alpha + \gamma'$) at ~300°C. See Figure 3. From the calculations of Chuang et al. (14), a miscibility gap (represented by dashed lines) extends from 9.0 to 51.5 wt. % Ni. Associated with this miscibility gap is a spinodal region at ~200°C located between 28.0 to 46.4 wt. % Ni. The spinodal boundaries are shown as cross-hatching. Compared to the diagram of Reuter et al. (15), the miscibility gap is larger and the spinodal region extends over the same range of nickel content.

At 50 wt.% Ni, the critical ordering temperature of the FeNi is at 350°C. Above this temperature, FeNi is disordered. A discrepancy between the diagrams of Chuang et al. (14) and Reuter et al. (15) is whether γ'' ($L1_0$ ordered FeNi) is in equilibrium with α. The presence of γ'' has been shown to exist contrary to the phase diagram proposed by Chuang et al (14). However, Reuter et al. (15) concluded from their meteoritic investigation that the γ'' is in equilibrium with the α. Yang et al. (17), on the other hand, concluded that at equilibrium, α and γ' are the only low temperature phases that are possible. Therefore, γ'' is considered a metastable phase by Yang et. al (17), and is represented as the dashed line that defines the high-Ni side of the miscibility gap in the phase diagram shown in Figure 3.

As stated previously, phosphides (schreibersite and rhabdite) and sulfides (troilite) occur in meteorites. The Arispe meteorite contains both inclusions. The effects of P and S are not important at the low temperature region of the Fe-Ni phase diagram. Their influences are only significant in the high temperature region (18).

C. Cooling Rates

Early calculations of cooling rates for iron meteorites were based on metallographic measurements of the Widmanstätten pattern. They are based on the kamacite bandwidth, profile matching or the Ni content. Wasson (19) formatted an equation which incorporated the bulk Ni content and the kamacite bandwidth.

A recent method proposed by Yang et al. (20) incorporates the "conventional" metallographic method and measurement of the cloudy zone in the plessite. This method can be applied to a vast number of iron, stony-iron, and stone meteorites.

D. Plessite

Plessite refers to the decomposed products in the retained taenite of a meteorite. It is a duplex structure of α and γ. It is not exactly clear as to what γ refers to. Plessite's size, structure and composition are all variable. The possible plessite structures which form are pearlitic (lamellar), spheroiditic, martensitic, microwidmanstätten α, acicular, comb, net, cellular, finger, black, and duplex. Examples of pearlitic and spheroidized plessite in the Arispe meteorite are shown in Figure 4.

Analysis with a microprobe across the retained taenite grain consistently reveals an M-profile, such as that shown in Figure 5 (5). The M-profile is formed as follows. As the temperature of the taenite decreases, kamacite nucleates on the octahedral planes of the taenite. The kamacite has a lower nickel content than the taenite. See Figure 6a and b. As the temperature continues to decrease, the nickel in the taenite can not diffuse to the center of the taenite grain to maintain equilibrium. The diffusion of the nickel is required to achieve equilibrium between the kamacite and the taenite. However, the center of the taenite grain now has less nickel than its

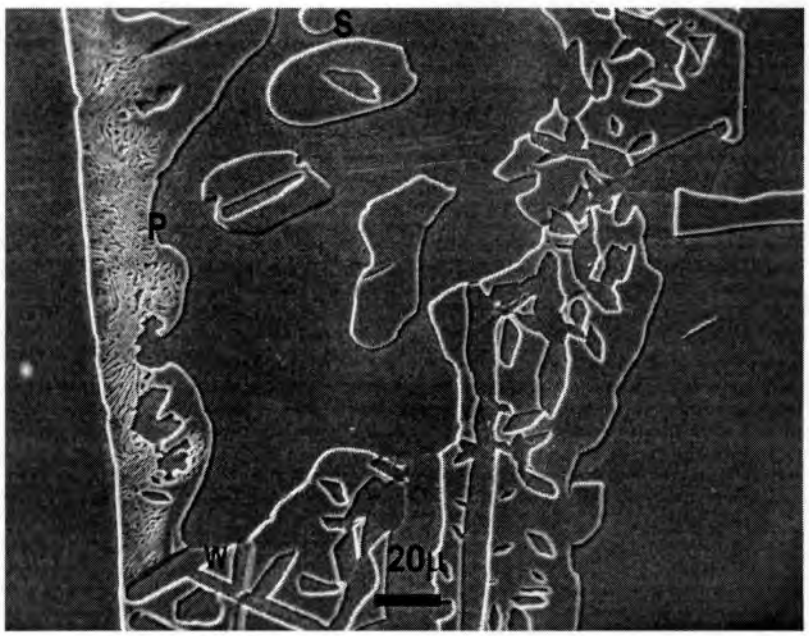


Figure 4. Taenite grain. Taenite grain showing pearlitic (P) and spheroiditic (S) plessite and a microwidmänstatten (W) pattern (21).

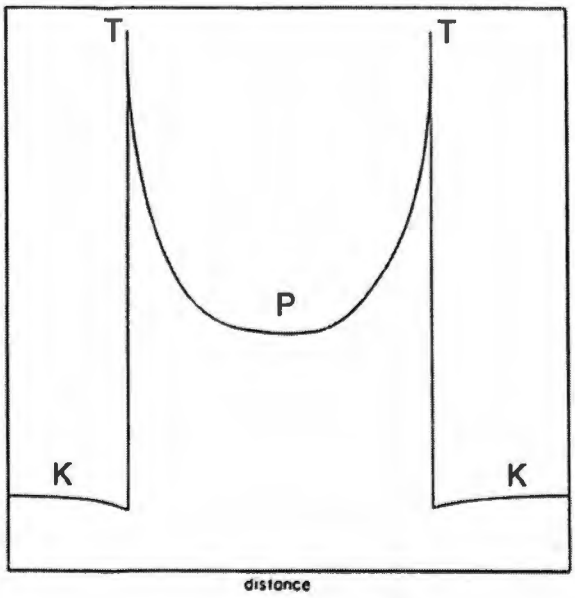


Figure 5. The M-profile. Kamacite (K). Taenite (T) Plessite (P) (5).

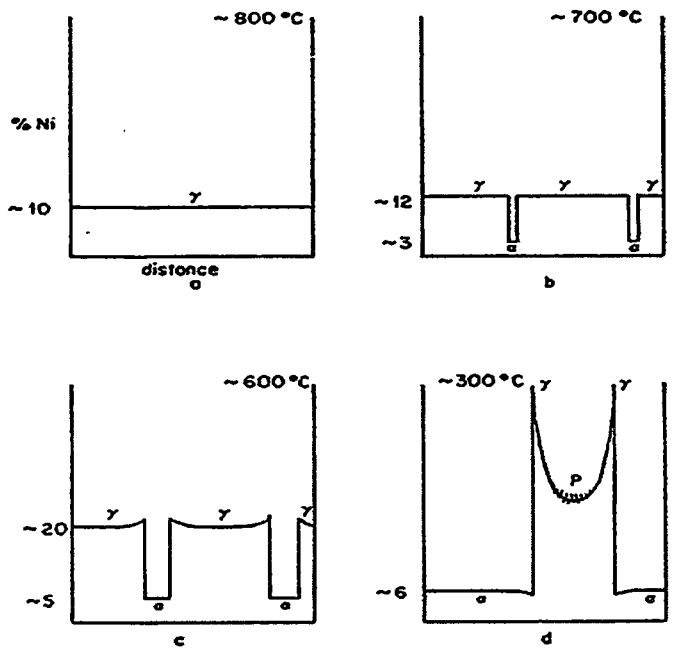


Figure 6. Formation of M-profile (5).

surrounding edges. See Figure 6c. Eventually, the temperature is now so low that movement of the nickel is nearly negligible. The resulting profile of the nickel content in the taenite is depicted in Figure 6d.

Although several variations in structure of plessite are known, four types, I, II, III, IV, are believed to form. Type I plessite is the result of the taenite cooling through the $\gamma/(\alpha+\gamma)$ boundary. The taenite continues to cool transforming to a $\alpha+\gamma$ mixture. Type II is formed when the taenite, after obtaining the M-profile, continues to cool and crosses the martensite (α_2) start temperature. The resulting phase would be a bcc phase that is of the same composition as the original taenite. Type III plessite is formed when the martensite decomposes to the $\alpha+\gamma$ phases, i.e $\alpha_2 \rightarrow \alpha+\gamma$. Type IV plessite contains a $\alpha+\gamma$ mixture and is found in high-Ni taenite (5). Despite the different paths on the phase diagram to obtain the M-profile, the resulting microstructures across the taenite are used to determine the Fe-Ni phase diagram. The formation of plessite will be commented upon further in the Discussion.

The M-profile, shown in Figure 5, can be further subdivided. With the use of Mossbauer spectroscopy, TEM and STEM, many studies of taenite and plessite have been done (13, 22-32). The high-Ni region, labeled as T in Figure 5, is taenite with microstructures that vary with the Ni gradient. It is therefore called zoned taenite. For example, Figure 7 is a schematic drawing of the high-Ni zoned taenite. In Figure 8, the region beside the kamacite (α) is the outer taenite rim, OTR. This area is further divided in three subzones, 1,2, and 3. Subzone 1 contains the phases Ni_3Fe and ordered FeNi (tetrataenite). Zones 2 and 3 also contain the tetrataenite and a bcc precipitate with low-Ni (α_2) . The final region is the cloudy zone which contains islands (I) in a honeycomb matrix (H). The island structure consists of FeNi and a bcc precipitate (α_2). The honeycomb matrix is a bcc structure (α_2). No distinction is stated as to the difference between the zones. Figure 8 shows a SEM image of the OTR and CZ in an iron meteorite. It is the OTR and the CZ that have been studied to determine the low temperature region of the Fe-Ni phase diagram.

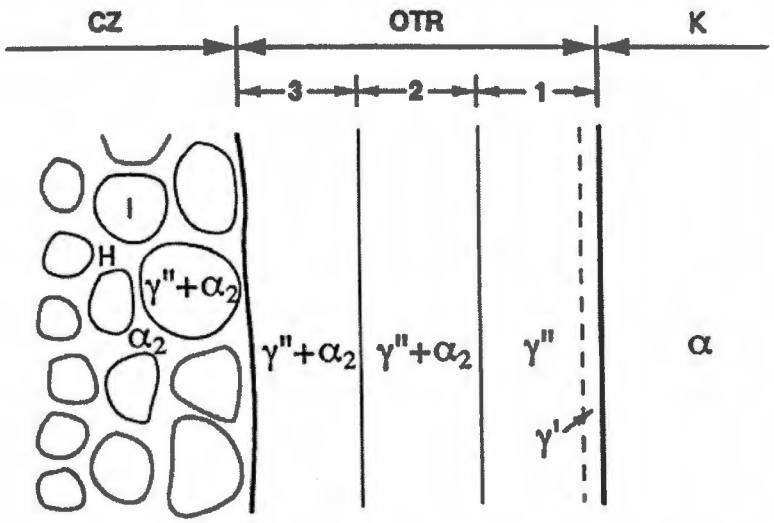


Figure 7. Schematic drawing of the zoned taenite. Honeycomb (H), Island (I), low-Ni precipitate (α_2) Ni_3Fe (γ``), Tetrataenite (γ`), Kamacite (α) (29).

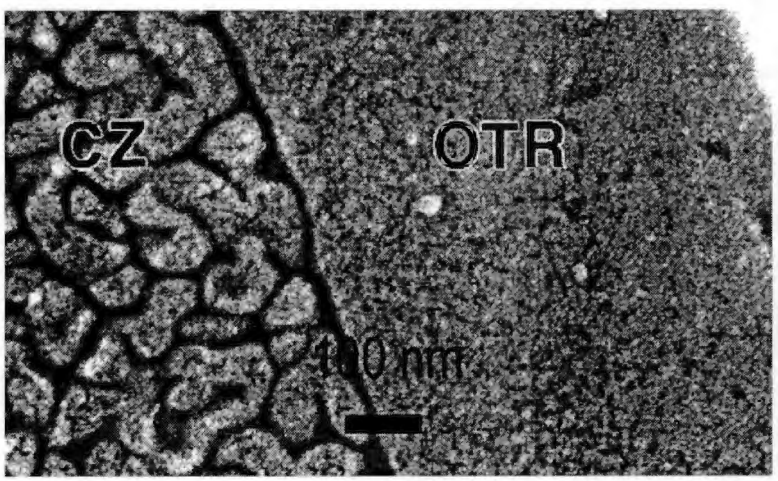


Figure 8. SEM image of OTR and CZ (13).

As mentioned previously and as shown in Figure 4, the plessite stringers in the Arispe meteorite can simultaneously contain the microwidmänstatten α structure and pearlitic (coarse and fine) and spheroiditic plessite (22, 24, 33). The phenomena of different plessites within the same grain has been noted in other iron meteorites (34). It is not clear how various plessite structures can occur within the same taenite grain, particularly since plessite morphologies depend on the iron meteorite's thermal history and the chemical composition.

Brooks and Perrin (35) observed that coarser pearlite in the Arispe and Odessa (Group IA) meteorites formed by a movement of a grain boundary into the finer pearlite. This grain boundary was determined to be a high-angle boundary. The coarsening of a lamellar structure by the movement of a high-angle grain boundary is called discontinuous coarsening (36). As shown by Brooks and Perrin (35), the coarsening of the pearlitic plessite at such low temperatures is possible due to the high diffusion rates associated with high-angle boundaries.

Brooks and DeMint (24) observed the spheroiditic and pearlitic plessite stringers in the Arispe meteorite. They noted that the spheroidized phase was austenitic and was high in Ni. Also noted was the formation of the spheroiditic phase at a ferrite boundary moving into the pearlite. Localized formation of the spheroiditic plessite was observed in the pearlitic plessite which may be the result of the localized thinning and thickening of the γ in the pearlitic plessite.

Brooks and Perrin (35) and Brooks and DeMint (24) suggest that the driving force for the coarsening and the spheroidization of the plessite may not be only the reduction of interfacial energy between the two phases, i.e. the α and γ. They state that the γ in the finer pearlitic plessite may be a metastable phase and may form an equilibrium phase (e.g., γ'') during coarsening .

V. Background of the Arispe Meteorite

The Arispe meteorite is named for the Mexican town near which it was discovered. The first find was in 1896, 25 miles northwest of Arispe. Sixteen individuals have been found on a 20 km line extending northwest from Arispe, Mexico. The largest of these individuals was 124 kg. The terrestrial age of the Arispe meteorite is estimated to be 240,000 +/- 50,000 years (21).

Structurally, the Arispe meteorite is classified as a coarse Octahedrite (Og) and is an Anomalous in the chemical classification. Figure 9 shows a specimen of the Arispe meteorite. The cooling rate has been calculated at >2°C/10^6 yr (8). The width of the kamacite bands is 2.9 +/- 0.5 mm. Original taenite individual crystals were as large as 25 cm in diameter. Buchwald (21) states that the Ni content is 6.7%. Other elements present are 0.45% Co, 0.3% P and traces of C, S, Cr, Cu, Zn, Ga, Ge, In, and Pt.

Neumann bands are numerous and vary with location. Troilite, scheibersite, and rhabdite have been observed as irregularly distributed. Cohenite nests have also been observed (21,22).

Plessite is not abundant (~2%). It is commonly observed as pearlitic. However, spheroiditic plessite and microwidmanstätten ferrite has been observed (21-24). Both pearlitic and spheroiditic plessite have been observed within the same taenite grain. The plessite and taenite are observed as thin stringers in the Arispe meteorite (21-24).

The M-profile of the Arispe meteorite was measured by Wood (36) and is shown schematically in Figure 10. Note that the OTR has a ~30% Ni content and the plessite has ~25% Ni. As seen in the Fe-NI phase diagram in Figure 3, no taenite phase with less than 50% Ni is predicted. It is unclear as to why the values in the M-profile are so low.

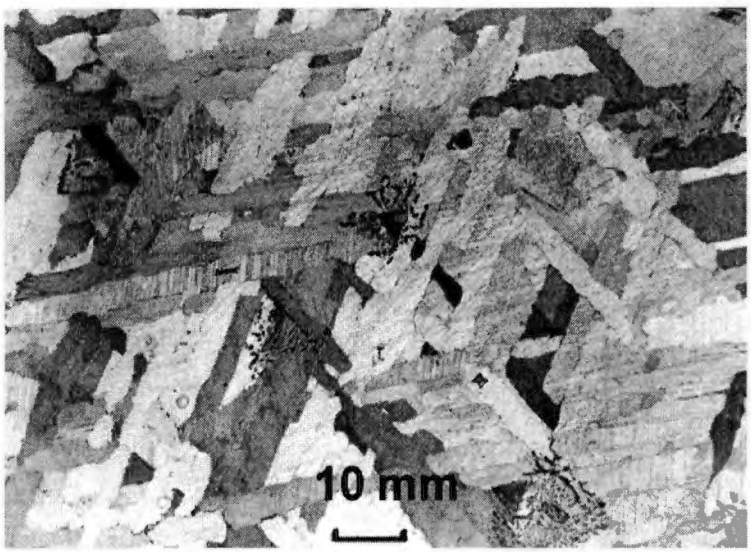


Figure 9. The Arispe Meteorite (21).

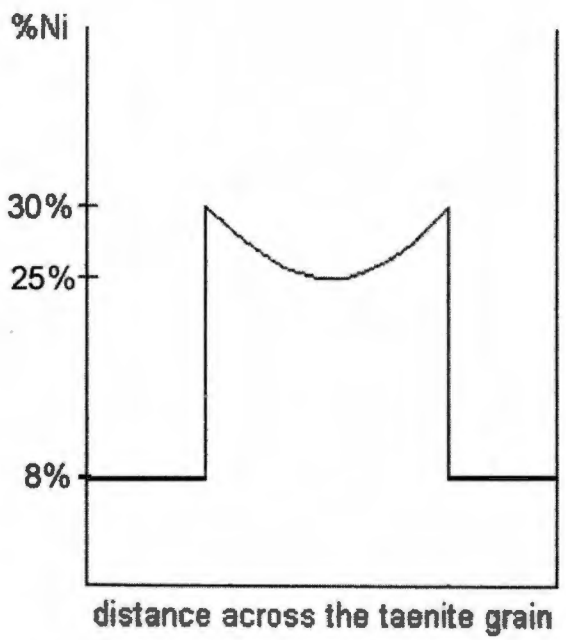


Figure 10. Schematic View of the M-Profile of Arispe Meteorite

VI. Experimental Procedure

Small Sections (~3cm x 1cm x 1cm) which had been cut from a large section of the Arispe meteorite were polished, etched and then inspected by optical microscopy for plessite stringers. A plessite stringer with a coarsening pearlitic microstructure was observed in one of these sections. From this section, two thin slices containing the plessite were removed with a thin blade, high speed cut-off wheel using copious water for cooling. These slices were then ground to approximately 0.025mm thick. The plessite stringer in each was marked with a pen, and a 3mm disk punched out with the plessite in the center. These two disks are referred to as Sample A and B.

Several 3mm diameter disks from a previous study (35) were observed in the optical microscope, and four were found to contain plessite stringers. These samples are labeled as C, D, E, and F. These samples contained a microwidmanstätten α structure.

All 3mm disks samples were electropolished in a Steuers® Tenupol-3 jet electropolisher. The electrolyte solution was:

730ml Ethyl Alcohol
100ml Butylcellosolve
90ml Distilled Water
78ml Perchloric Acid

The solution was water cooled at ~20°C. The electropolishing voltage was set to 15-120v, as recommended by the manufacturer for polishing iron. The photosensitivity was initially set at the most sensitive setting in order to obtain the smallest hole possible.

The hole produced by electropolishing in Sample C had no areas at the rim of the hole that were transparent to electrons. It was then ion milled for 4 hours with the beam at 20°, but it was still too thick. The beam angle was lowered to 18° and the specimen ion milled for two hours, producing areas of appropriate thickness for TEM observations.

Figure 11 shows a typical specimen. The plessite stringer (of microwidmanstatten ferrite) extends across the hole produced by the electropolishing of the primary ferrite. Along the edge of

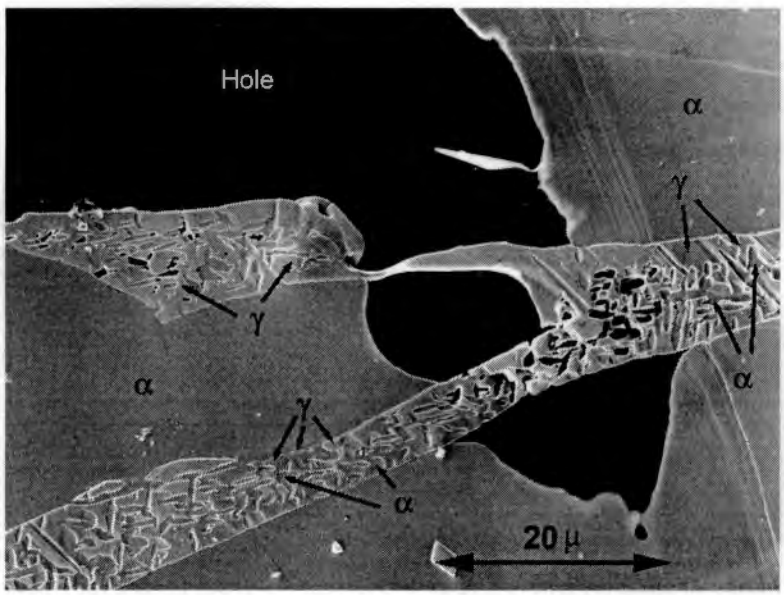


Figure 11. TEM Sample of Microwidmanstätten Structure.

the plessite, the structure was sufficiently thin for TEM observations. After making TEM observations of such specimens, the disks were briefly (e.g., 2 sec) electropolished further in attempts to produce additional thin areas for observations. This was successful only occasionally.

Once a hole had formed in the plessite stringer, the specimen was placed immediately in a Hitachi H-800 TEM/STEM operated at 200kv. If an area within the plessite was sufficiently thin, bright field (BF) images, Selected Area Diffraction Patterns (SADP), and energy dispersive spectra (EDS) using a Link Pentafet X-ray detector were obtained. An example of the spectra obtained by EDS is shown in Figure 12. Although other weak peaks such as P and Cu (from the specimen holder) were generated, only the Ni and Fe peaks were used in the analysis.

The values of the chemical composition obtained by analyzing the EDS must be used with caution. This is a result of one or a combination of the influences of the following factors on the analysis of the EDS. a) If the α overlaying any γ is not removed, then the analysis from regions which appear to be only γ is affected by the underlying α. b) The software used to analyze the spectra to obtain chemical analysis is valid only for thin foils. If the region being analyzed is too thick, then absorption and fluorescence affect the EDS spectra and must be taken into account. c) Cu peaks due to the x-rays generated from the sample holder.

The percentages of Fe and Ni were calculated directly using the peak integrals which the analysis program supplied from the spectra. The integrals were summed and divided into the values for each element to obtain the atomic percentage of Fe or Ni.

Images of the surfaces of the areas of the specimens from which SADP and EDS spectra were obtained were taken with STEM. Since these were of limited quality, the specimens were subsequently examined in a SEM, and better quality images were obtained of the same areas. These were used to identify regions analyzed.

The crystal structure of α is body-centered cubic (bcc) and that of the high-Ni phases (e.g., γ, γ') is based on the face-centered cubic structure. Thus, indexing the SADPs was

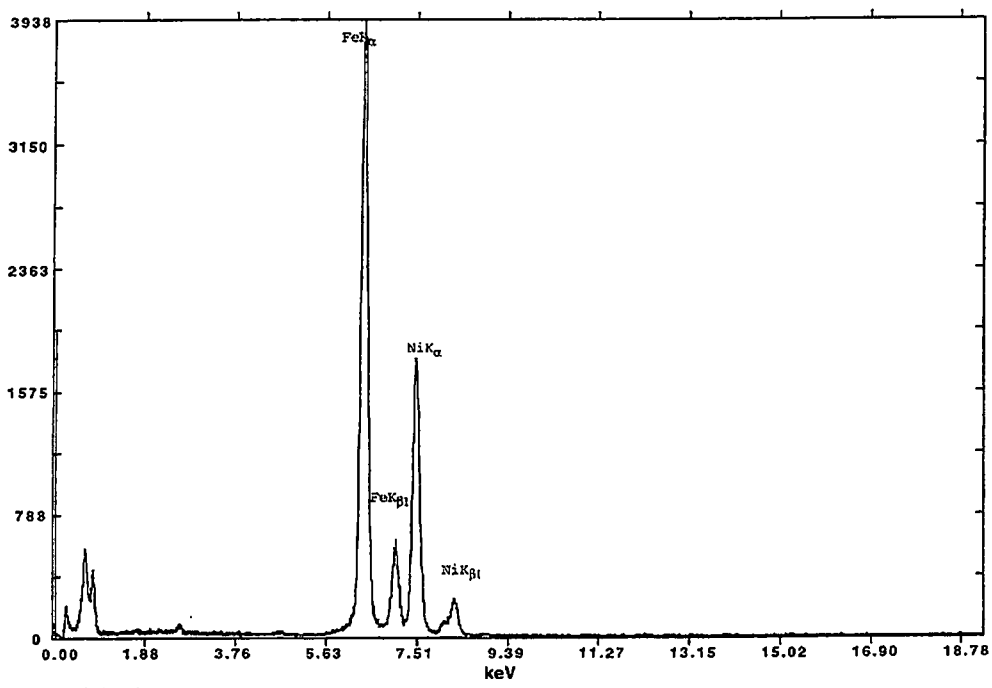


Figure 12. An example of the EDS spectra obtained.

relatively simple. Once the SADPs were indexed, the zone axis for each SADP was calculated. Using the program Difpat EGA Version 2.01 or MacTempas, the zone axis from the SADPs were entered into the program to obtain a calculated diffraction pattern for ferrite or tetrataenite. The main task was to determine whether regions of high Ni were disordered or ordered. The expectation was that ordered tetrataenite might be present, so the diffraction patterns of this structure were examined. This phase has the $L1_0$ structure, which is shown in Figure 13. Ni atoms are at the locations (0,0,0) and (½,½,0) and Fe atoms are at (0,½,½) and (½,0,½). Superlattice spots are present for certain patterns. However, variants may not show such spots, either because they are forbidden or because they are very weak. An example is seen in examining <110> patterns. Figure 14b shows the [110] pattern, where prominent {001} superlattice spots are noted by the arrows. The crystal arrangement in Figure 14a shows clearly why these reflections are present, as the (100) planes are alternating pure Fe and pure Ni. However, the orientation shown in Figure 15a shows a [101] pattern in which the {001} spots are missing, and the atom arrangement in Figure 15b shows why. Thus, the lack of clear superlattice spots in SADPs does not preclude the presence of an ordered structure. Other variants of the zone axis must be examined.

Distances to prominent spots on the SADPs were measured and these were used to calculate the lattice parameter. The values of the lattice parameter had approximately 10% error.

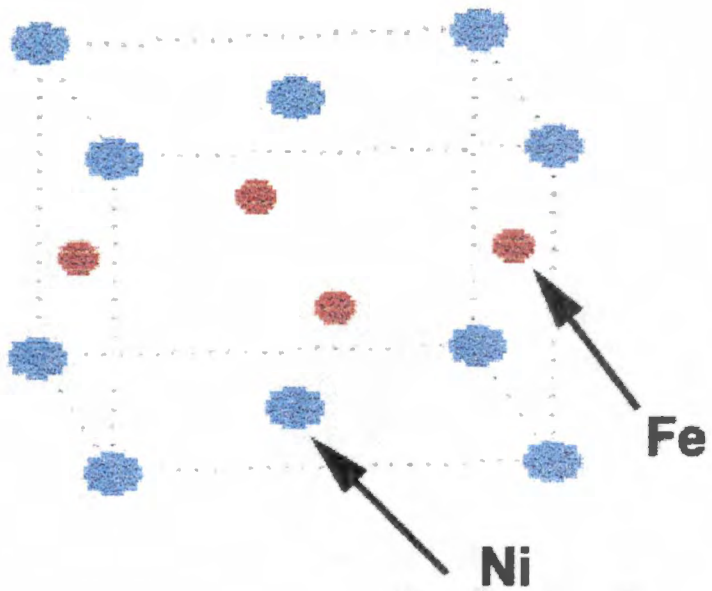


Figure 13. Cubic Structure of Tetrataenite.

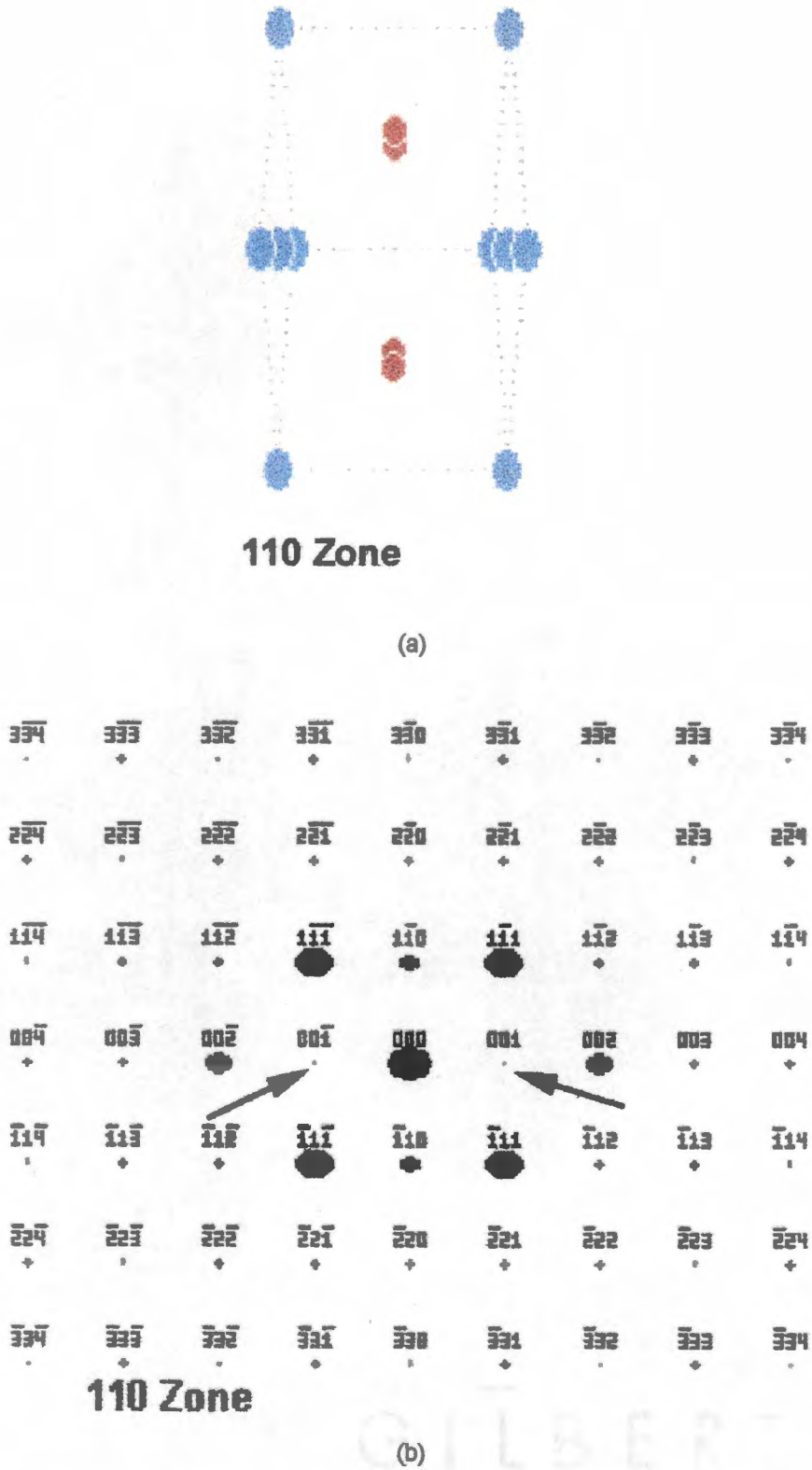
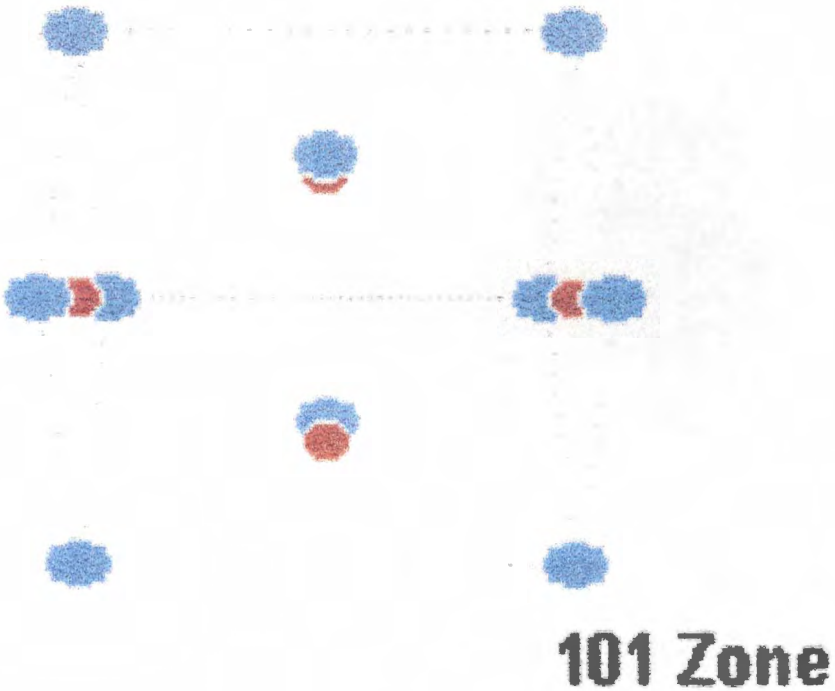
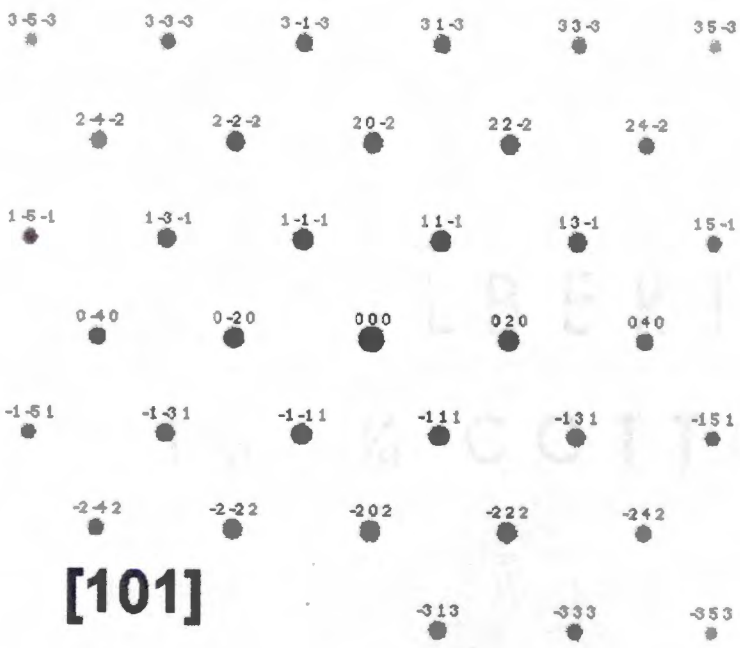


Figure 14. (a)Tetrataenite crystal oriented to a [110] zone axis. (b) The diffraction pattern calculated for a [110] zone axis of tetrataenite.



(a)



(b)

Figure 15. (a)Tetrataenite crystal oriented to a [101] zone axis. (b) The diffraction pattern calculated for a [101] zone axis of tetrataenite.

VII. Results

The results of the TEM observations of the Arispe meteorite are discussed according to the microstructure of the plessite in the stringer. The microstructures that were observed were pearlite, microwidmanstätten α, and martensite. In the images that follow, the kamacite and taenite phases are sometimes annotated with arrows. The generic symbol, γ, is utilized for the taenite phase, but this by no means indicates whether the phase is taenite or tetrataenite. α denotes the kamacite phase. Unless otherwise noted, the calculated diffraction patterns are for tetrataenite and are determined using the zone axis of the SADP.

The lattice parameters of Fe-Ni ferrite and austenite as a function of composition were determined by Owen and Sully (36). The values are approximately 2.86 A for α and 3.58 A for γ, and are essentially independent of Ni content. The lattice parameter of austenite and tetrataenite (3.65 A (37)) are similar. For each SADP, the lattice parameter was calculated, and is shown on the SADPs presented here. The values have an error of about 10% which is sufficiently small to distinguish α from taenite or tetrataenite. However, the parameters of γ and tetrataenite are too close to distinguish these two phases from this information alone.

The phase which was etched was α, and it always had low Ni content from the EDS analysis (e.g., 5% Ni). Also, SADPs from these regions were indexed as from a body-centered cubic structure and the calculated lattice parameter always agreed with the known values for α. The regions which were not etched always had an EDS analysis which was high in NI, usually about 48% Ni. Where SADPs were obtained, the patterns were indexed as either face-centered cubic or tetrataenite. The lattice parameters calculated from the patterns agreed with those of γ or tetrataenite. Note that the only direct proof that tetrataenite was present was observation of SADPs with superlattice spots.

Sample A of the Arispe meteorite contained a stringer with pearlitic plessite that was coarsening and spheroiditic plessite. An SEM image from that plessite stringer can be seen

in Figure 16. Area A of Figure 16 is shown in Figure 17. Figure 18a, 18b, and 18e are TEM images from the region of Area A noted in Figure 17. The SADPs in Figures 18c and 18f were obtained from the locations noted in Figure 18a. The calculated diffraction patterns are shown in Figures 18d and 18g. Indexing determined that the zone axis for both of these SADP's was <110>. Note that the superlattice spots are not present in the SADP shown in Figure 18g, but are in Figure 18d. Recall that for the tetrataenite structure superlattice spots will be present in a [110] pattern, but not in [101] or [011] patterns. Thus the lack of superlattice spots in Figure 18f does not prove that the region from which this pattern came was not tetrataenite. Although no EDS spectra were obtained from this region, the observation of superlattice spots indicates that these plates are tetrataenite.

Figure 19 is an SEM image of Area B in Figure 16, and Figure 20a is a TEM image of this area. The SADPs (Figs. 20b and 20c) are from the areas noted. Note the agreement between the SADP and the diffraction pattern calculated for the bcc structure. EDS revealed that these areas contained low Ni, ~<7%. Agreement between the observed and calculated diffraction patterns and the chemical composition confirms these noted areas to be kamacite. Also, the lattice parameter calculated from the SADP agrees with the lattice parameter of kamacite from the literature.

The γ plate noted in Figure 19 contained ~42% Ni, but this area was not thin enough for a SADP. However, a γ plate in a nearby area was sufficiently thin and the two SADPs obtained from this area are shown in Figures 21a and 22a. The calculated diffraction patterns in Figures 21b and 22b are for tetrataenite. The Ni content for these selected areas was ~50%, suggesting that these areas are tetrataenite. There are no superlattice spots in the SADPs in Figures 22b and c. The calculated diffraction pattern in Figure 21b shows two superlattice spots that are not seen in Figure 21a. The absence of superlattice spots in the SADP may be due to crystallographic orientation.

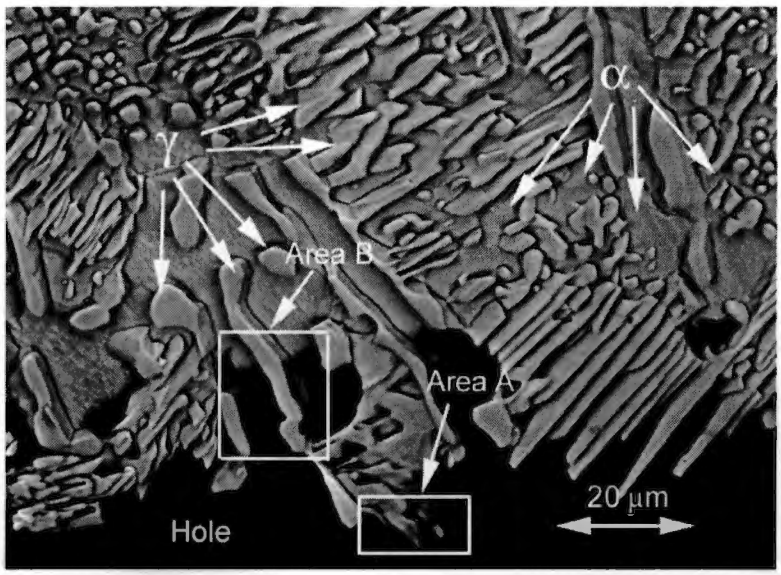


Figure 16. SEM image of Pearlitic Plessite from Sample A.

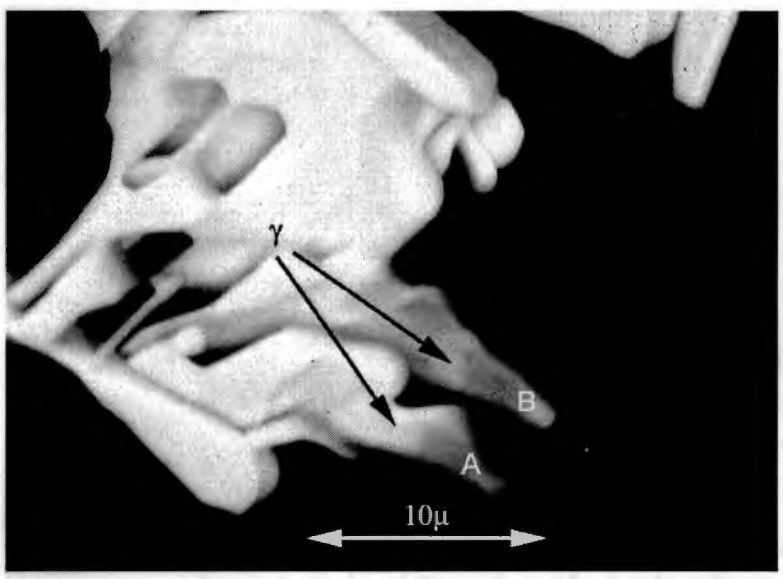
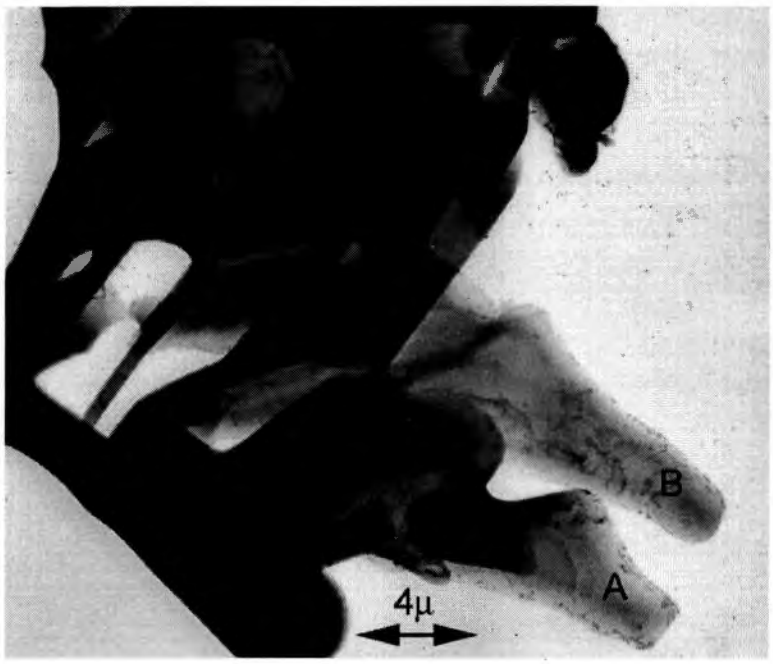
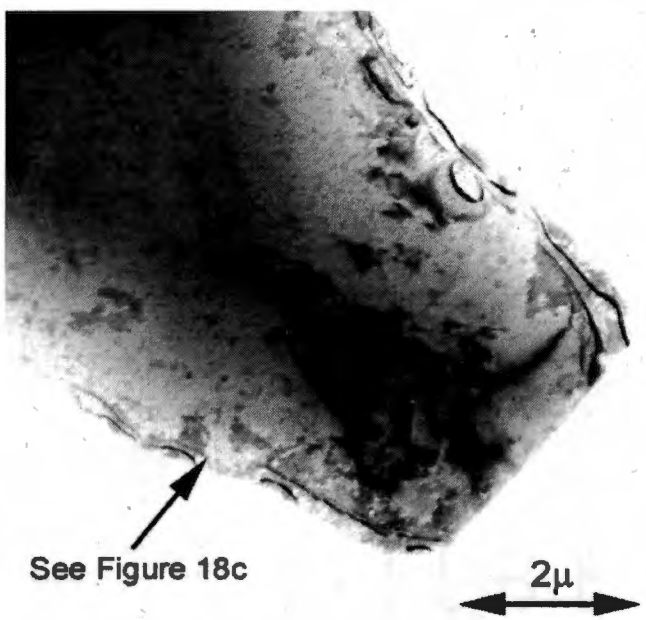


Figure 17. SEM image of Area A in Figure 16.

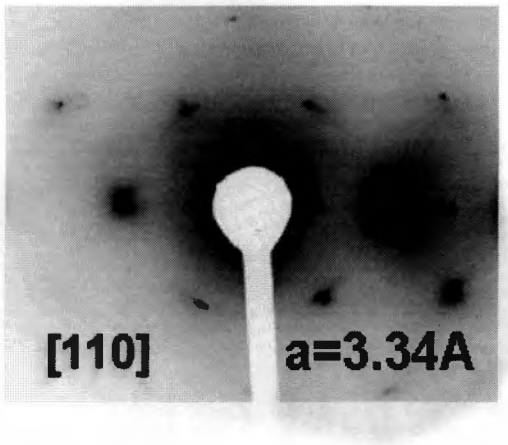


(a)

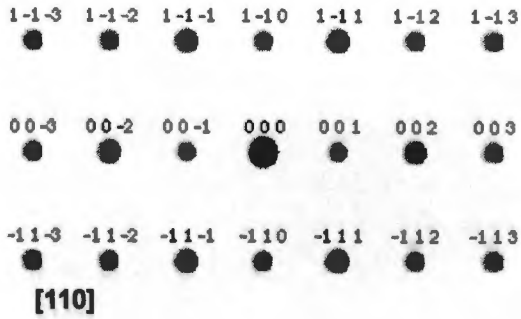


(b)

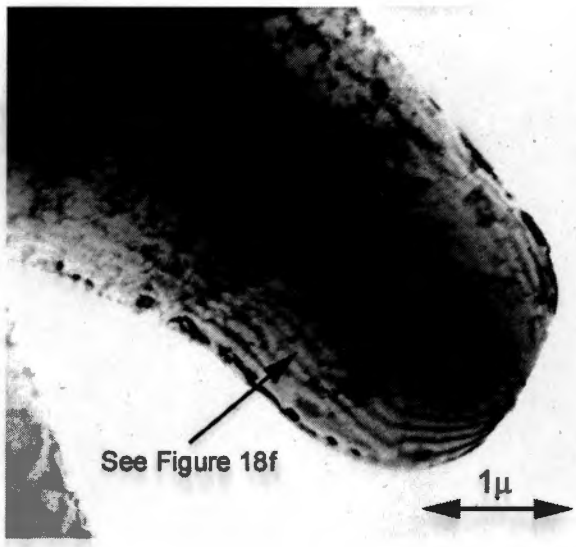
Figure 18. TEM Observation of γ Plates. (a) BF image of Area A in Figure 16. (b) BF image of plate A in Figure 18b. (c) SADP of Area A in Figure 18b. (d) Calculated diffraction pattern of [110] zone axis of γ". (e) BF image of Area B in Figure 18b. (f) SADP of Area B in Figure 18e. (g) Calculated diffraction pattern of [101] zone axis of γ".



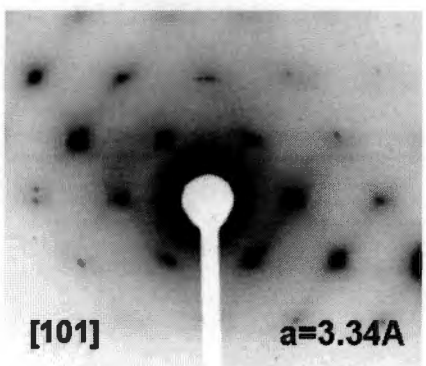
(c)



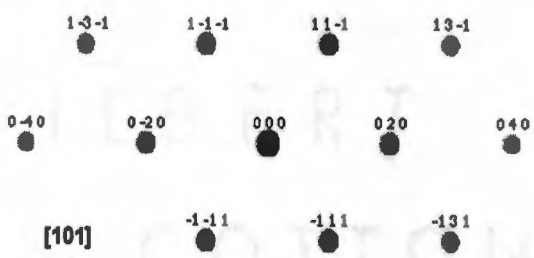
(d)



(e)



(f)



(g)

Figure 18. (continued)

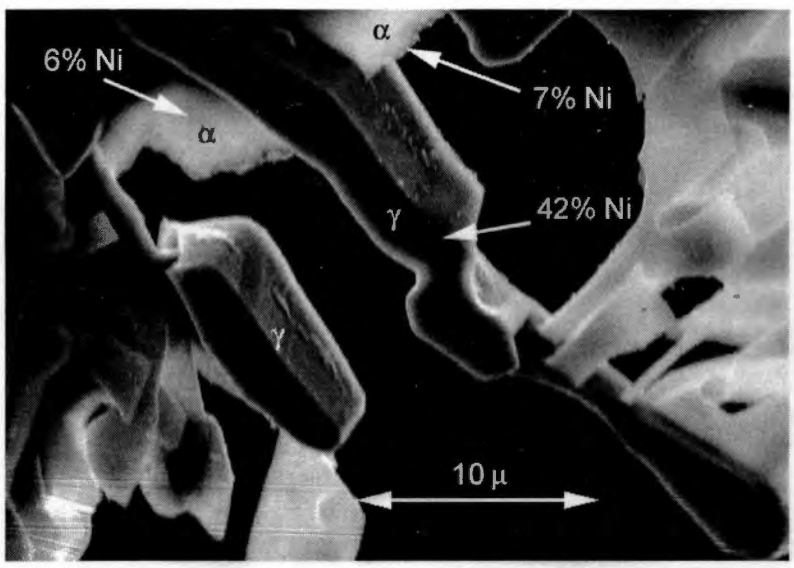
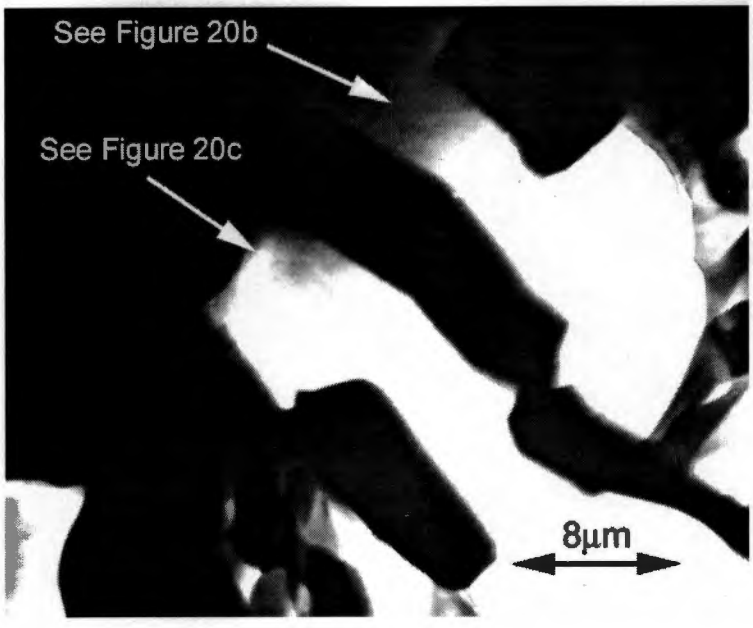
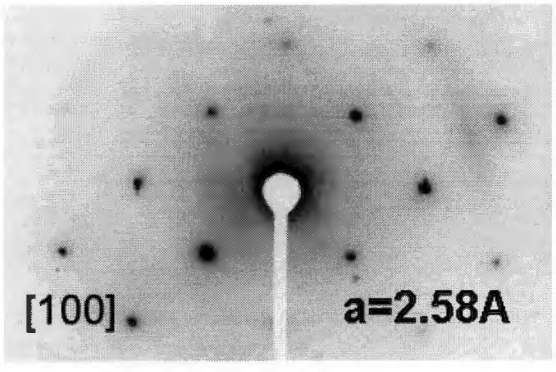


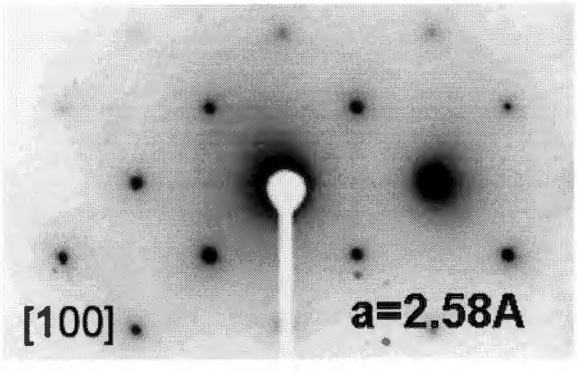
Figure 19. SEM image of γ plate and α from TEM Sample A.



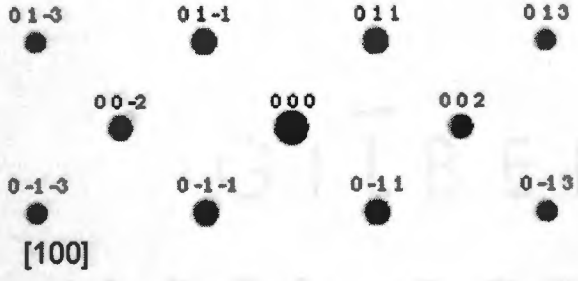
(a)



(b)



(c)



(d)

Figure 20. TEM observation of α. (a) BF image of Figure 19. (b) SADP from noted location in (a). (c) SADP from noted location in (a). (d) Calculated diffraction pattern for a <100> zone axis of a bcc structure.

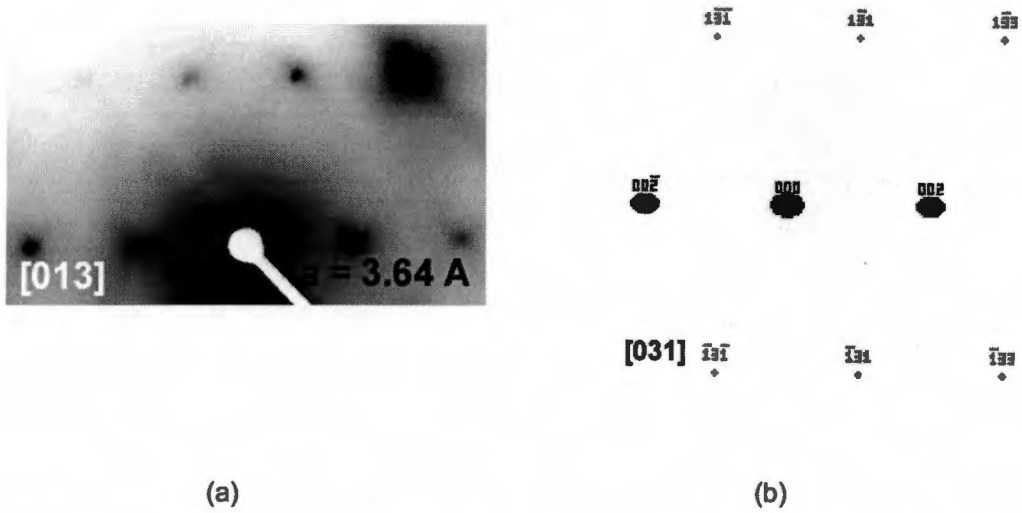


Figure 21. Diffraction Pattern of γ Plate from Sample A.
(a) SADP of γ plate. (b) Calculated diffraction pattern for a [013] zone axis of γ".

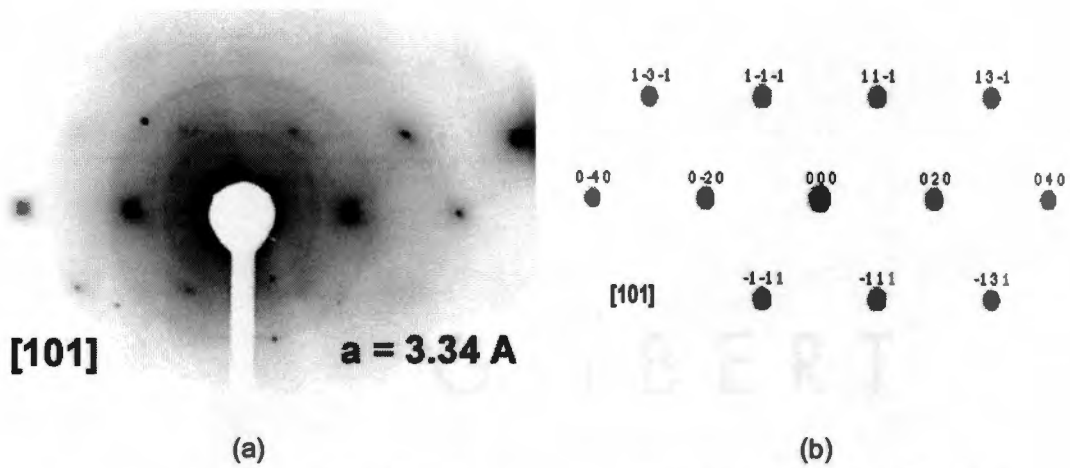


Figure 22. Diffraction Pattern of γ Plate from Sample A.
(a) SADP of γ plate. (b) Calculated diffraction pattern for a [101] zone axis of γ".

Another region of the pearlitic plessite from Sample A is shown in Figure 23. A TEM image of Area A in Figure 23 is shown in Figure 24a. The SADP and the calculated diffraction pattern are shown in Figure 24b and 24c, respectively. As can be seen in Figure 24a, the Ni content varied along the γ plate. The difference may be due to two factors. One factor is the removal of less α during the electropolishing in one area versus another. The second factor may be that the γ plate may gain in thickness further from the hole. Thin foil specimens are optimum for EDS analysis. The plates in this region may be too thick for the EDS analysis to be accurate since the beam does not penetrate the sample. It can not be concluded that the plates are tetrataenite since no superlattice spots were observed in the SADP.

Near the pearlitic plessite shown in Figure 23, the TEM image shown in Figure 25a was obtained. A SADP from the region noted is in Figure 25b. Figure 25c is the calculated diffraction pattern. No superlattice spots can be seen in the observed and calculated diffraction patterns. The Ni content was 50% at the tip of the plate, but lower away from the edge of the hole. This is probably due to the effect of the neighboring α, which had a Ni content of about 7%. It can not be concluded that the γ plates from this region are tetrataenite due to the lack of superlattice spots in the observed and calculated diffraction patterns.

Figure 26 shows a region in the lamellar structure which is coarsening. The tips of the γ phase were not sufficiently thin for SADPs. However, EDS showed that the γ contained 50% Ni and the α 5% Ni. The Ni content of these tips supports the speculation that the plates are tetrataenite, since it will contain approximately 50% Ni.

Figure 27a shows another pearlitic plessite from Sample A. This region can be seen to be coarsening like the region shown in Figure 26. Figure 27b is an SEM image of Area A in Figure 27a. Figure 28a is a TEM image of one of the γ plates in Figure 27b. It is difficult to match the Figures 28a and 27a, which is the result of the sample being inverted in the SEM holder. The sample was never rotated to verify if the inversion resulted in the mismatch of the

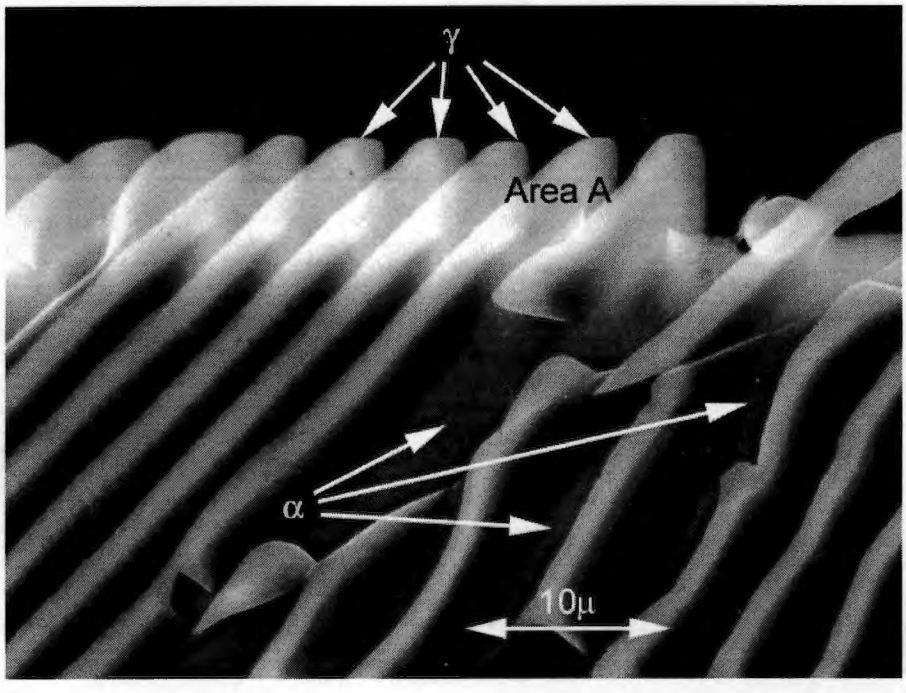
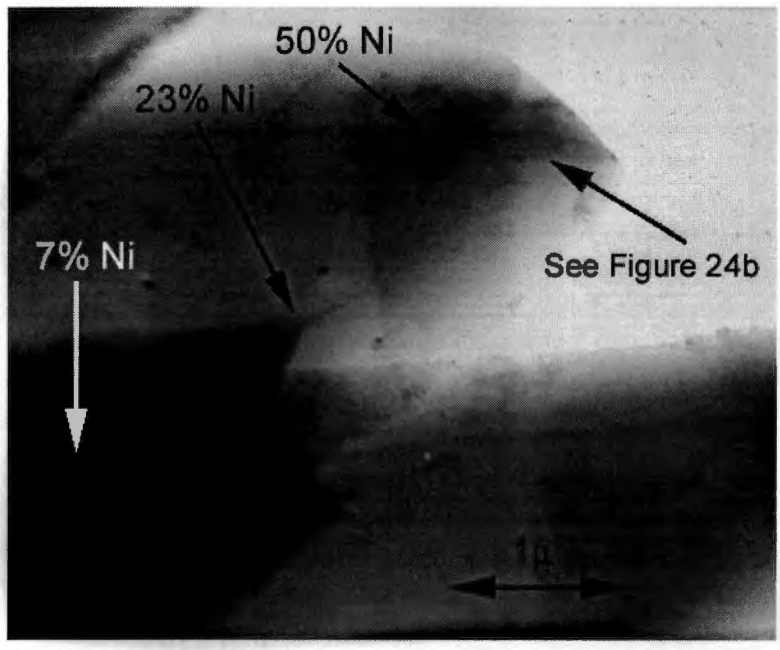
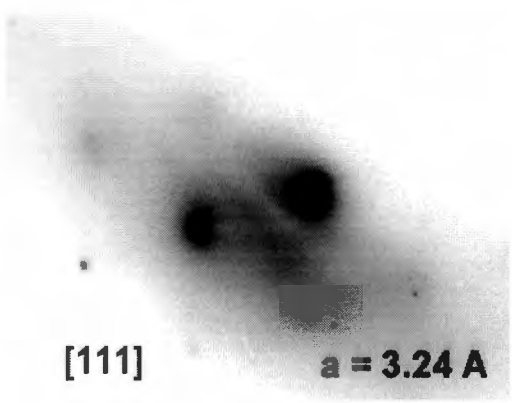


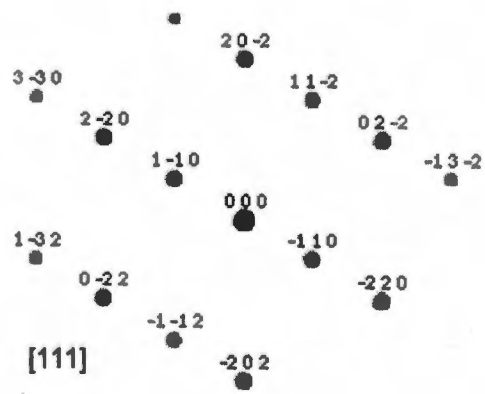
Figure 23. SEM image of Pearlitic Plessite from Sample A.



(a)

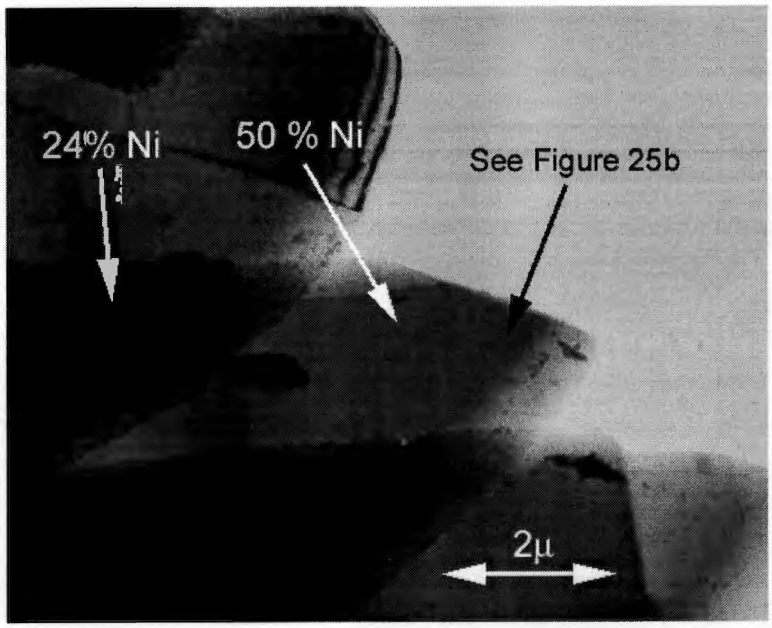


(b)

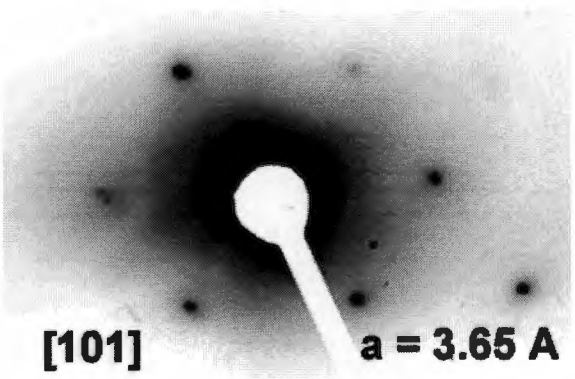


(c)

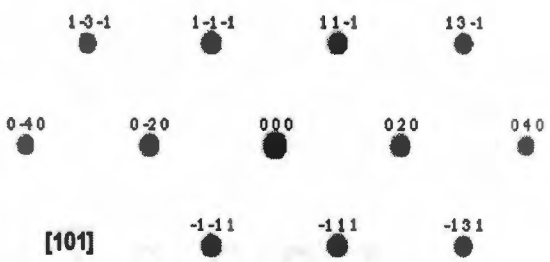
Figure 24. TEM Observation of γ Plate. (a) γ plate from Sample A. (b) SADP from noted area in (a). (c) Calculated diffraction pattern for a [111] zone axis from γ".



(a)



(b)



(c)

Figure 25. TEM Observation of γ Plate. (a) γ plate from Sample A. (b) SADP from noted area in (a). (c) Calculated diffraction pattern for a [101] zone axis from γ".

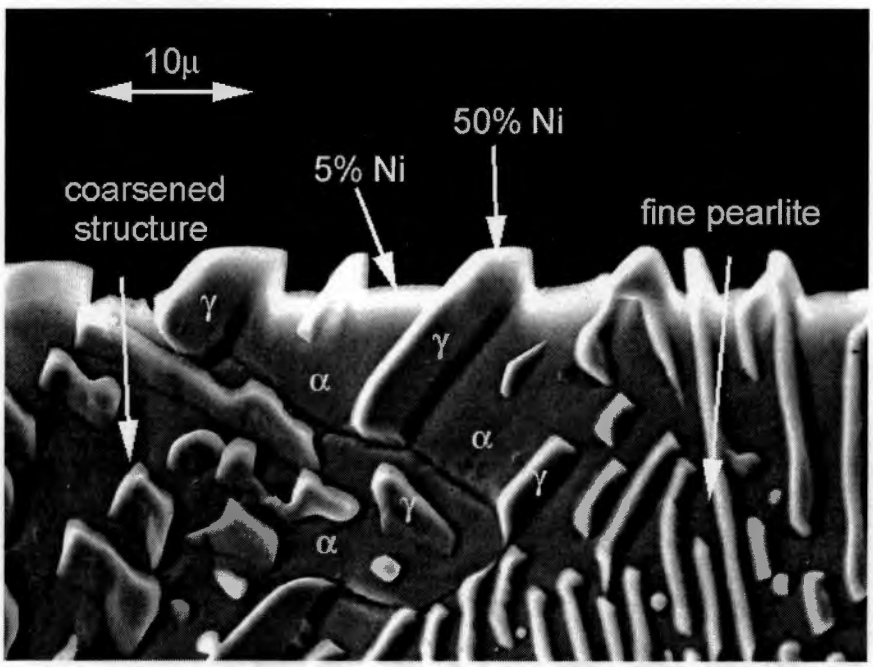
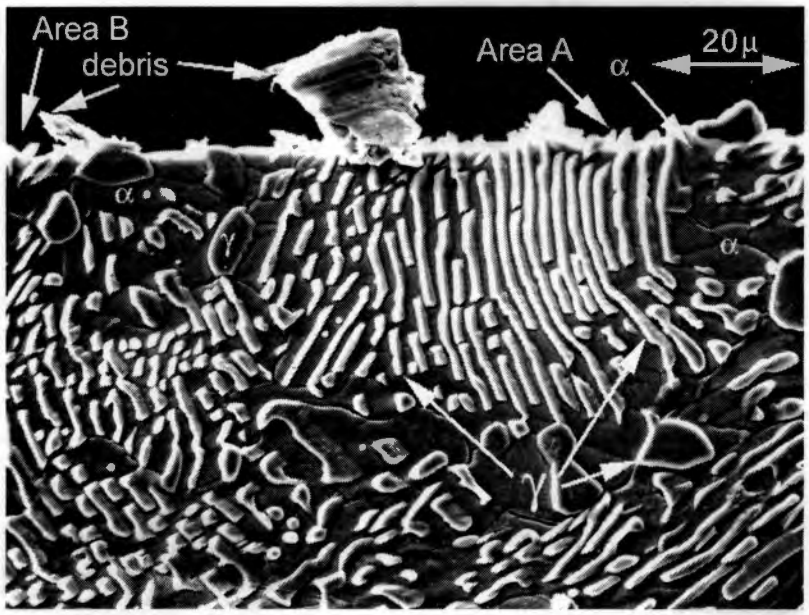
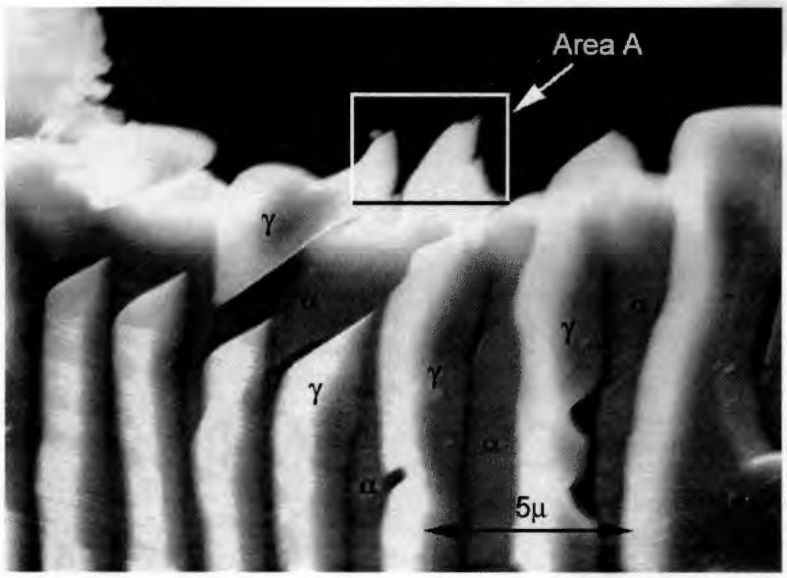


Figure 26. Coarsening Pearlitic Plessite from Sample A.

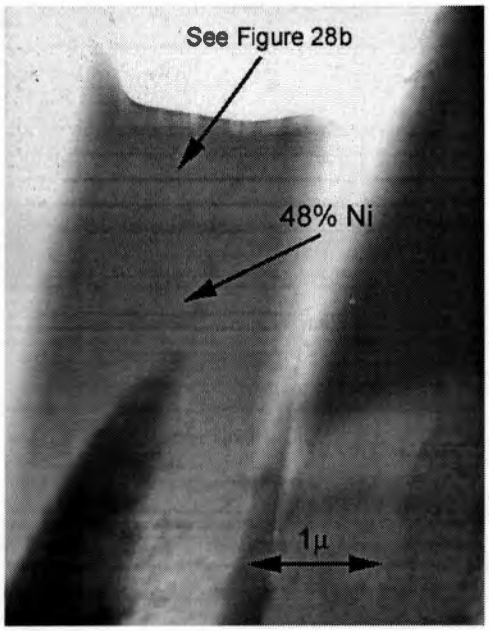


(a)

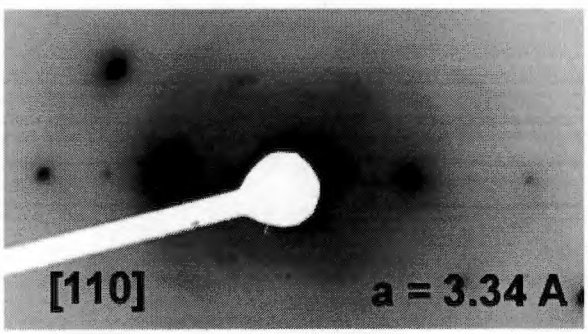


(b)

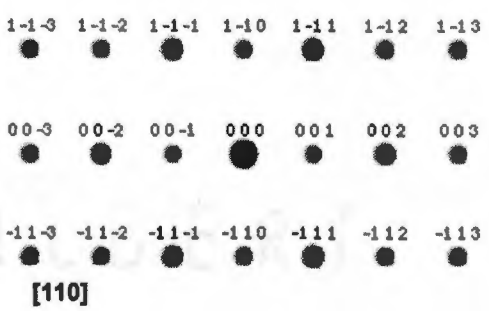
Figure 27. SEM Images of Pearlitic Plessite
(a) SEM image of pearlitic plessite from Sample A.
(b) SEM image of Area A in (a).



(a)



(b)



(c)

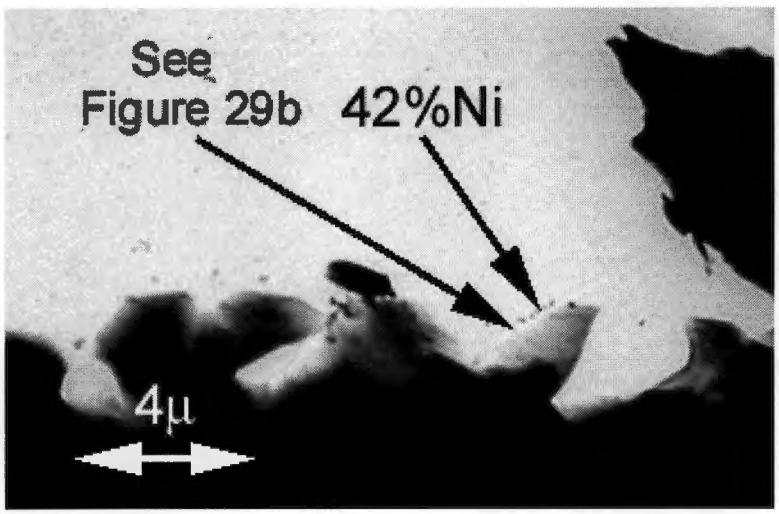
Figure 28. TEM Observation of γ Plate. (a) γ plate from Area A in Figure 27 (b). (b) SADP from noted area in (a). (c) Calculated diffraction pattern for a [110] zone axis from γ".

images. Figure 28b is the SADP from the region noted in Figure Ma and the calculated diffraction pattern is shown in Figure 28c. Note the appearance of the superlattice spots in both figures. The TEM image in Figure 29a and the SADP in Figure 29b are from Area B in Figure 27a. EDS analysis of the γ from these areas noted gave a Ni content of ~48%. The superlattice spots in the SADP and the Ni content of 50% from this area show that it is tetrataenite.

Two other regions of the pearlitic plessite from Sample A are shown in Figures 30a and 31a. SADPs from these regions are shown in Figures 30b and 31b, and the calculated diffraction patterns are shown in Figures 30c and 31c. Note the difference in Ni content obtained by EDS. Both the observed and calculated diffraction patterns show no superlattice spots. Therefore, it is inconclusive whether these regions are tetrataenite.

Figure 32a shows pearlitic plessite in Sample B. A SADP is shown in Figure 32b, and calculated pattern in Figure 32c. EDS found the Ni content to be 47%. Although this area has a Ni content as high as tetrataenite, it can not be determined if this is tetrataenite due to the lack of superlattice spots in the observed and calculated diffraction patterns.

Sample C contained a stringer with a microwidmanstätten α structure, as shown in Figure 33. As noted in Figure 33, the Ni content varies along the sample's edge. This variation may be due to the previously mentioned factors that influence the EDS analysis. A TEM image, SADPs and calculated diffraction patterns for this sample are shown in Figure 34. Figures 34b and f are SADPs from the high Ni regions in Figure 33. The lattice parameter calculated from these SADPs agrees with that of the known lattice parameter. The SADP in Figure 34d is of the low Ni region, α. Calculation of the lattice parameter confirms this area to be α. The TEM images in 35a and 36a are also of the microwidmanstätten α structure in Sample C's stringer. As seen in Figure 35a, the α had low Ni content and the Ni content of the each γ plate was variable. This variation may be the result of the EDS analyzing the plate and the α that may lie beneath the plate. However, the SADP in Figure

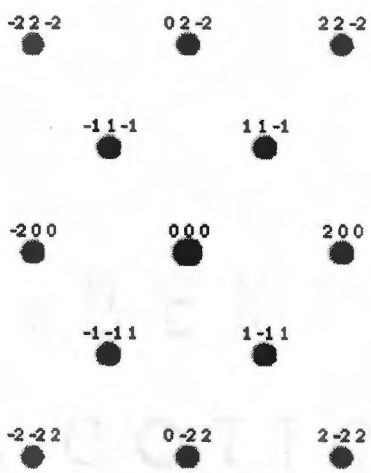


(a)



[011] a = 3.30 A

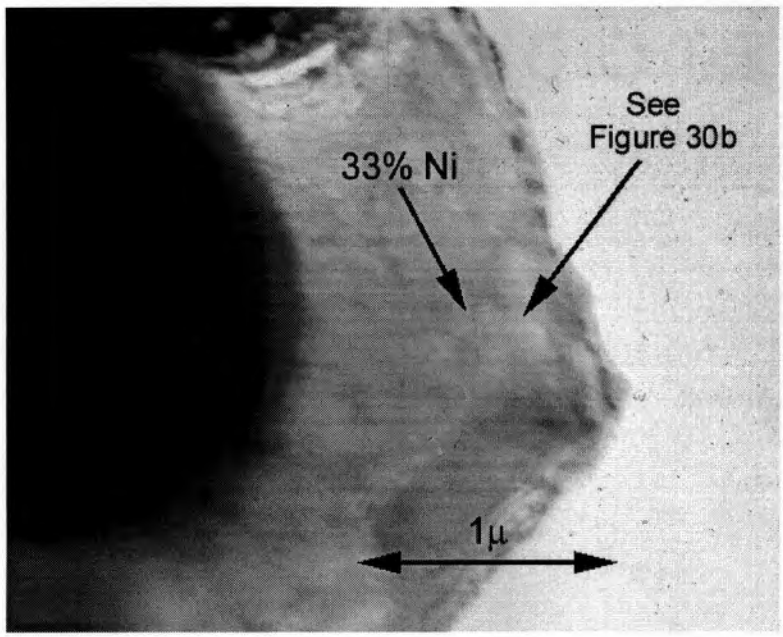
(b)



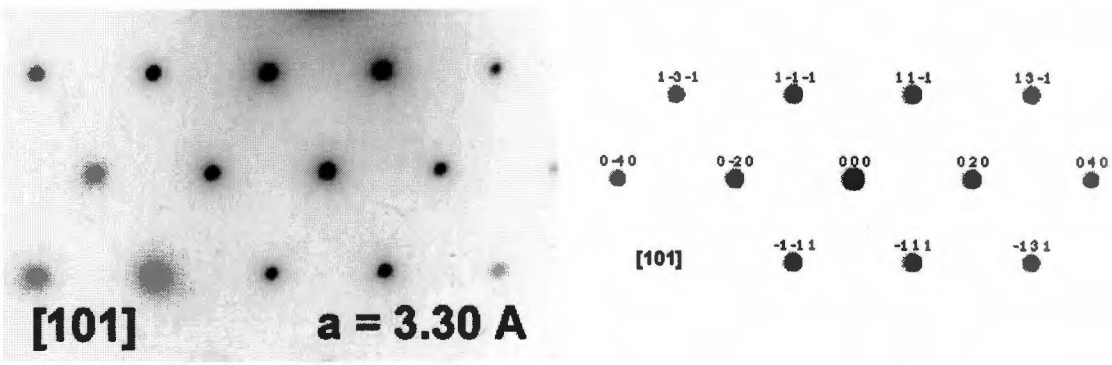
[011]

(c)

Figure 29. TEM Observation of γ Plate. (a) γ plate from Sample A..
(b) SADP from noted area in (a). (c) Calculated diffraction pattern for a [011] zone axis from γ".



(a)



(b) (c)

Figure 30. TEM Observation of γ Plate. (a) γ plate from Sample A..
(b) SADP from noted area in (a). (c) Calculated diffraction pattern for a [101] zone axis from γ".

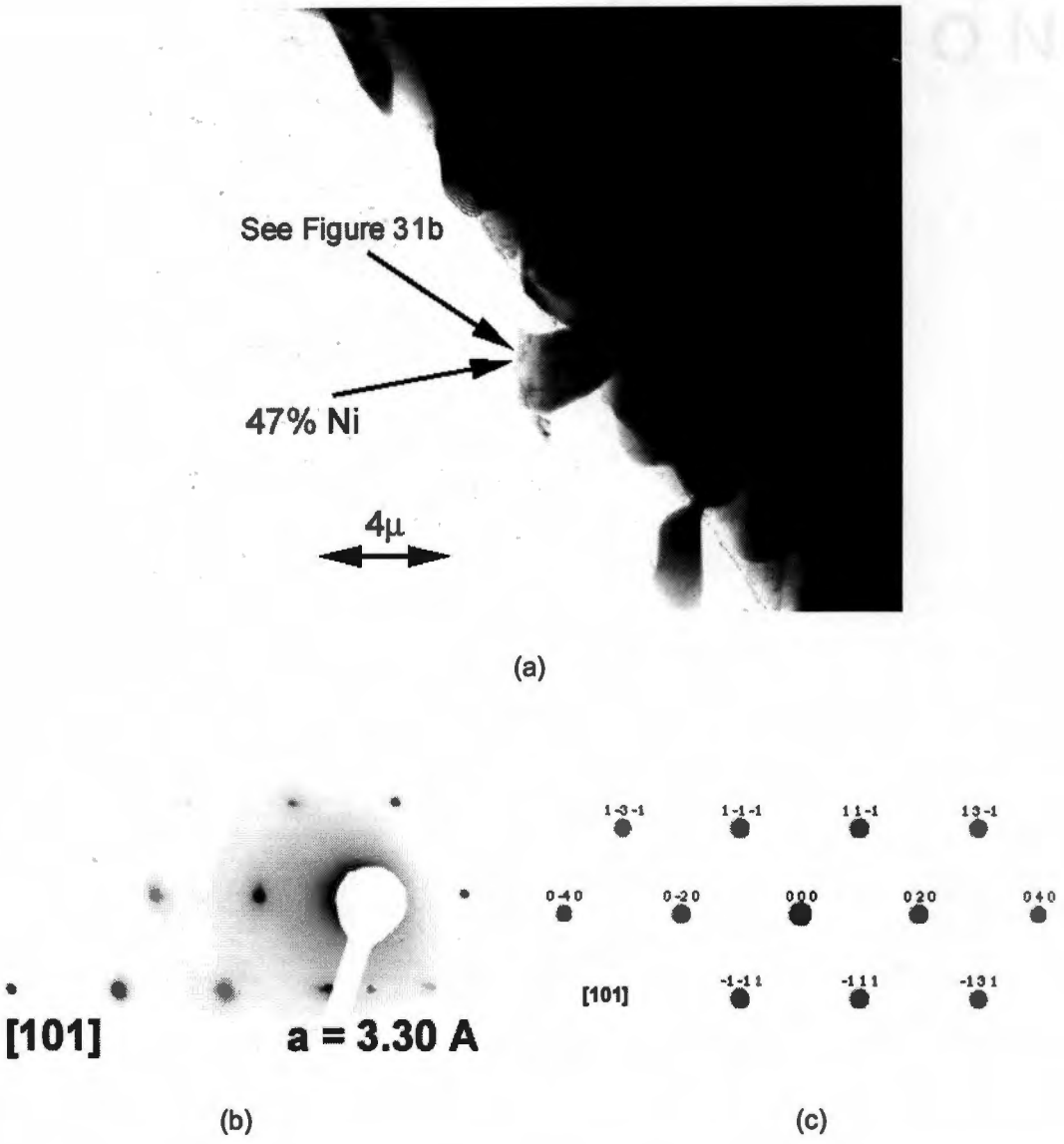
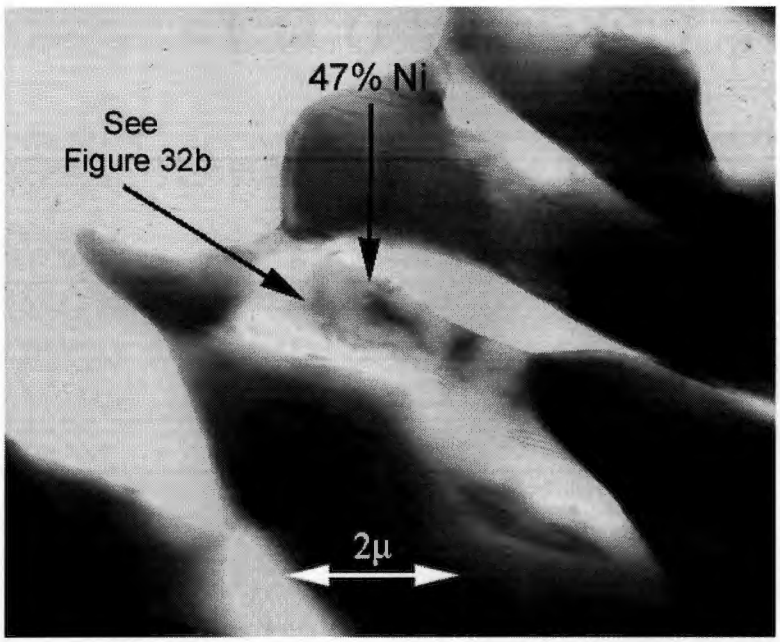
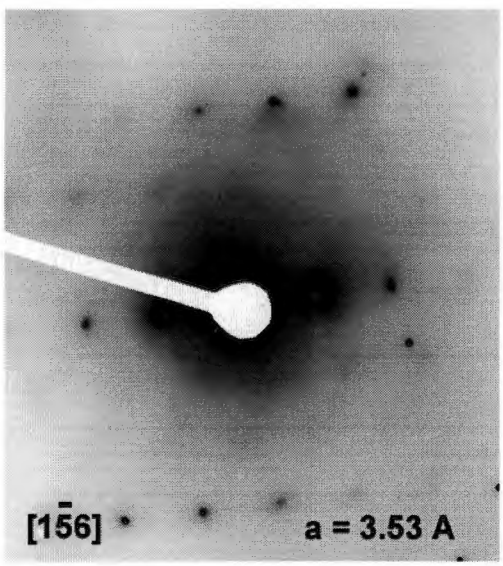


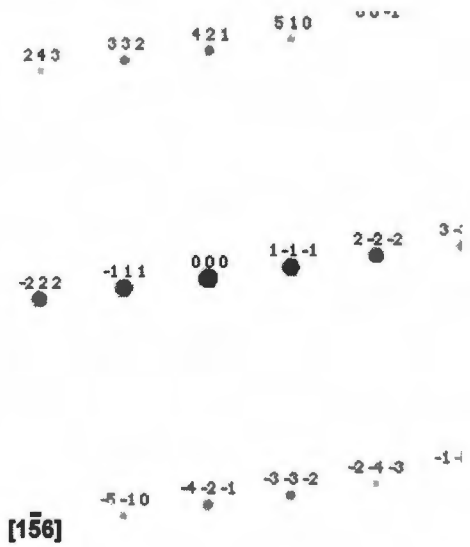
Figure 31. TEM Observation of γ Plate. (a) γ plate from Sample A..
(b) SADP from noted area in (a). (c) Calculated diffraction pattern for a [101] zone axis from γ".



(a)



(b)



(c)

Figure 32. TEM Observation of γ Plate. (a) γ plate from Sample B. (b) SADP from noted area in (a). (c) Calculated diffraction pattern for a [156] zone axis from γ".

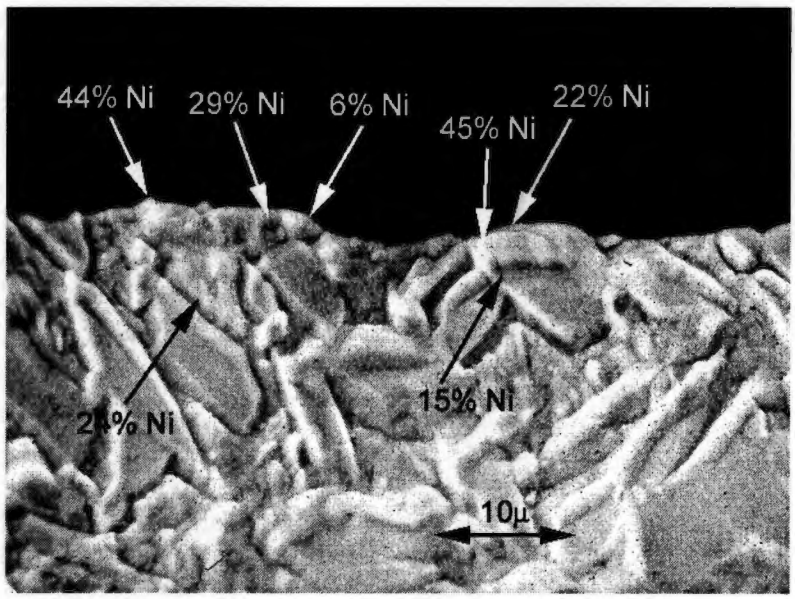
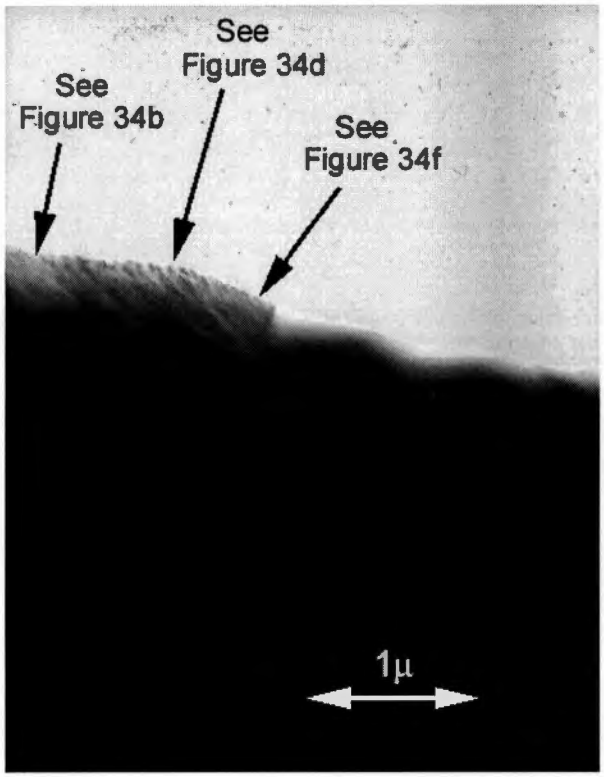
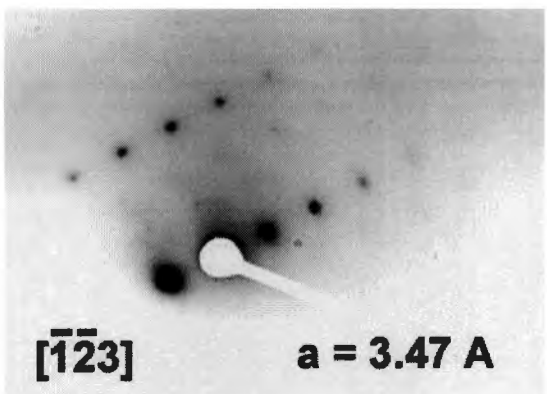
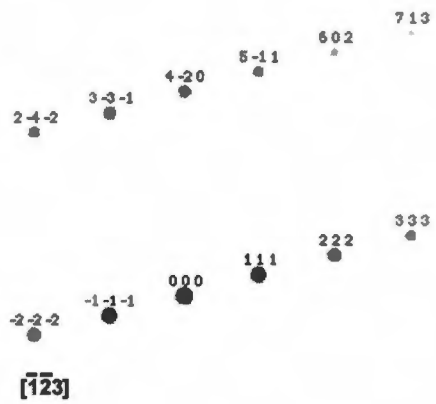


Figure 33. SEM Image of Microwidmanstätten α Structure in Sample C.



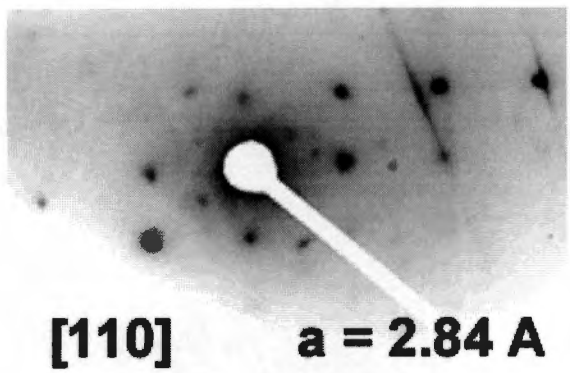
(a)

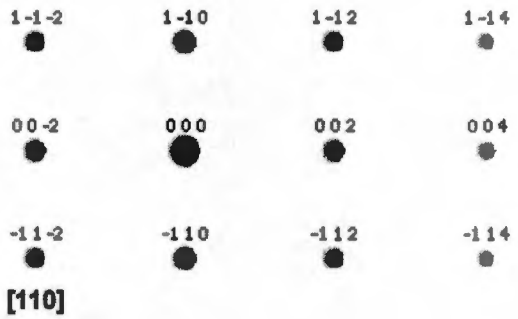




(b) (c)

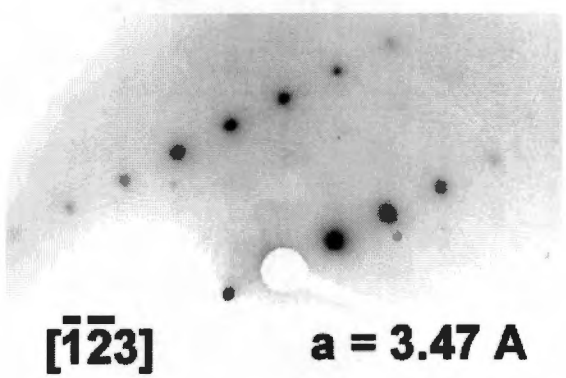
Figure 34. TEM observation of Microwidmanstättan α Structure. (a) TEM image of microwidmanstätten structure from Sample C. (b) SADP from noted area in (a). (b) Calculated diffraction pattern for [123] zone axis of γ". (c) SADP of noted area in (a). (d) Calculated diffraction pattern of a [100] zone axis for a bcc structure. (f) SADP from noted area in (a). (g) Calculated diffraction pattern for [123] zone axis of γ".

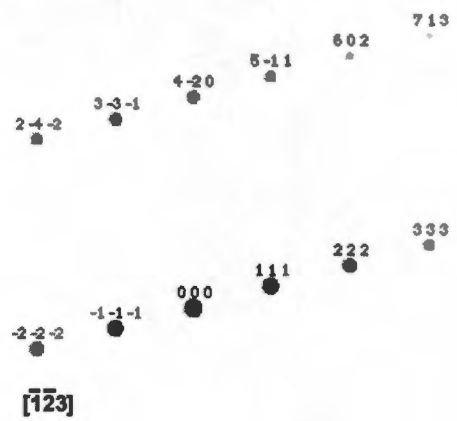




(d)

(e)

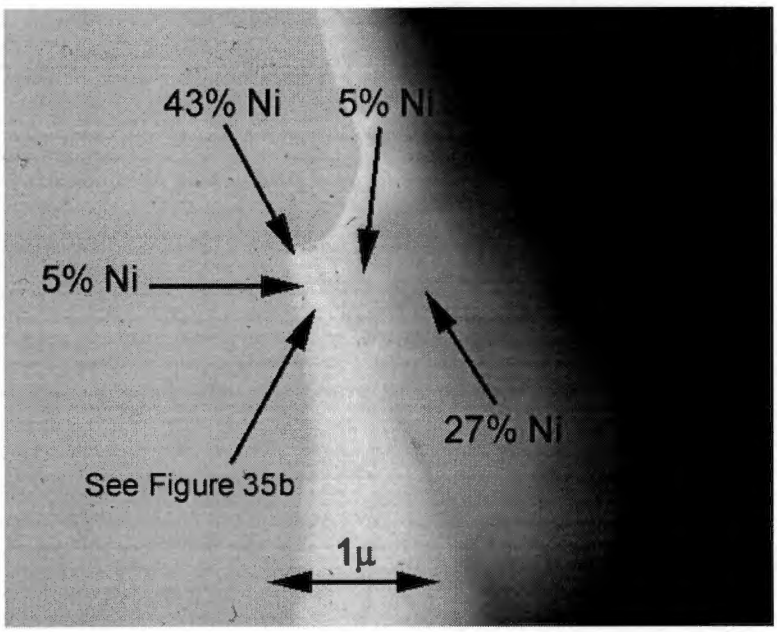




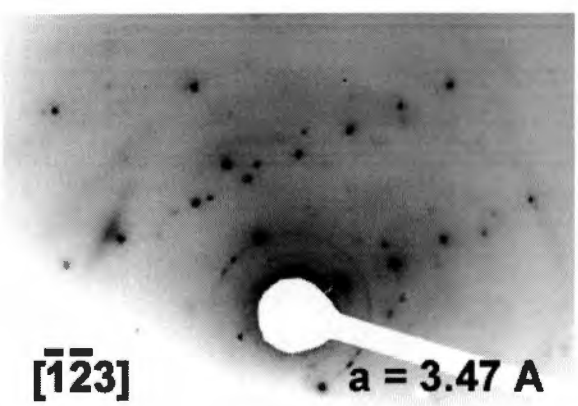
(f)

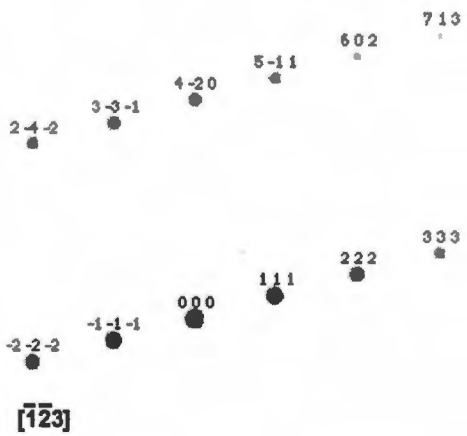
(g)

Figure 34. (continued)



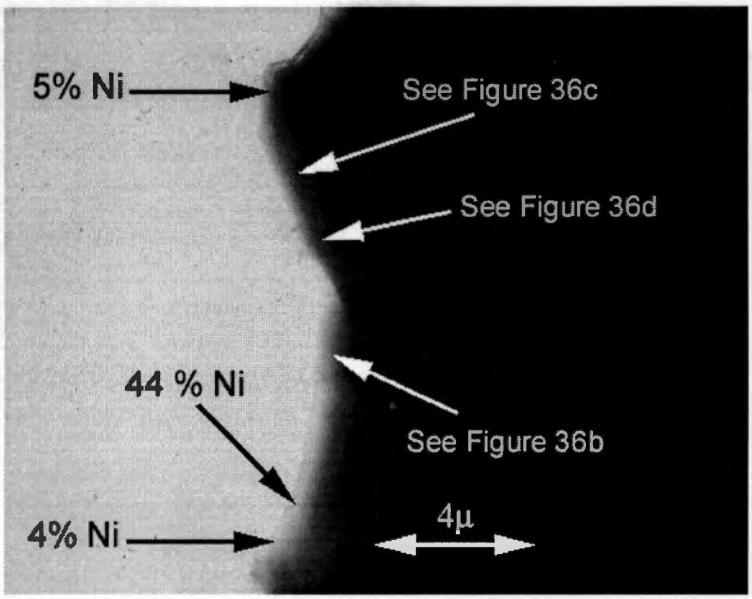
(a)



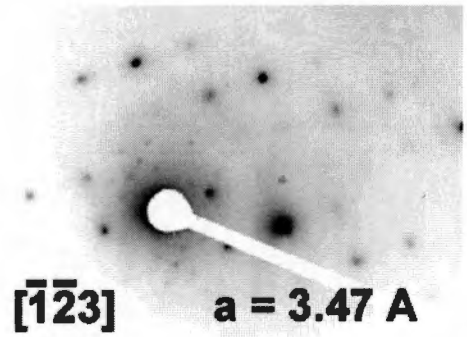


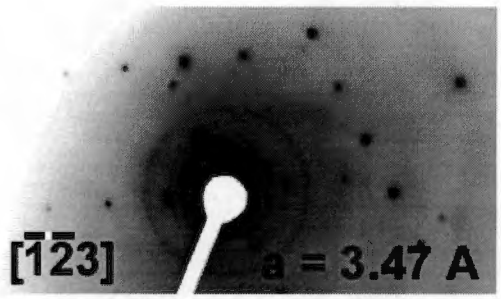
(b) (c)

Figure 35. TEM Observation of Microwidmanstätten α Structure. (a) TEM image of microwidmanstätten structure (b) SADP from noted area in (a). (c) Calculated diffraction pattern for a [123] zone axis from γ". Note that other spots may be due to debris or a nearby γ plate.



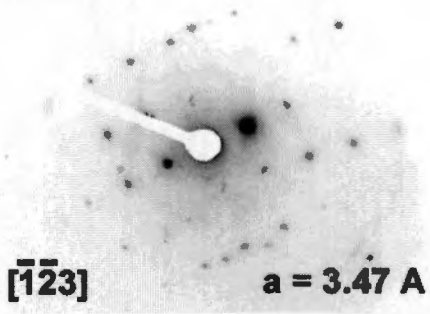
(a)





(b)

(c)





(d) (e)

Figure 36. TEM Observation of Microwidmanstätten α Structure. (a) TEM image of microwidmanstätten structure (b) - (d)SADP from noted area in (a). (e) Calculated diffraction pattern for a <123> zone axis from γ". Note that other spots in SADPs may be due to debris or a nearby γ plate.

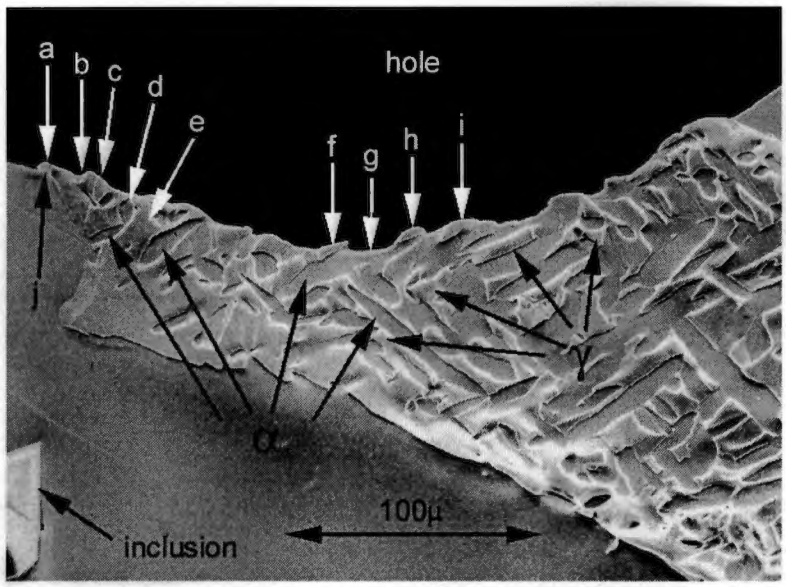
35b correlates well with the calculated diffraction pattern in Figure 35c. SADPs were obtained from the microwidmanstätten α structure shown in Figure 36a. See Figures 36b, c, and d. These SADPs (Figures 35b and 36b) also correlate well with the calculated diffraction patterns (Figures 35c and 36d), although the lack of superlattice spots prevents any conclusion as to the identification of this area. The Ni content of the γ was the same for both areas, ~44%, with some variations in other plates due to factors previously discussed.

A stringer from Sample D with a microwidmanstätten α structure is shown in Figure 37a. Although the α and the γ were not sufficiently thin for any TEM observations, EDS analyses were obtained. The results for specific locations noted in Figure 37a are shown in Figure 37b. The Ni content of the α was what should be expected, according to the Fe-Ni phase diagram. However, the γ regions were not sufficiently high in Ni content to be tetrataenite. This may be due to the influences on EDS analysis of factors mentioned previously.

Another region in Sample C was sufficiently thin for TEM observation of the α within the stringer. See Figure 38. The calculated diffraction pattern (see Figure 38c) is for the [111] zone axis of a bcc structure. Agreement between the calculated and known lattice parameter, in conjunction with the EDS analysis, proves this area to be kamacite.

The primary α around the stringer of Sample D was thin enough for the TEM observations made in Figure 39a. The software was unable to calculate the zone axis [7-3 15] of this SADP. Calculation of the lattice parameter agrees with that of the lattice parameter of kamacite.

Sample E contained another stringer with the microwidmanstätten α structure shown in Figure 40. The α and the γ in the stringer were not thin enough for any TEM observations, but EDS analyses were performed. At locations noted in Figure 40, the Ni content was ~21%. Like previous samples, this Ni content may be influenced by what is beneath the γ plates. No

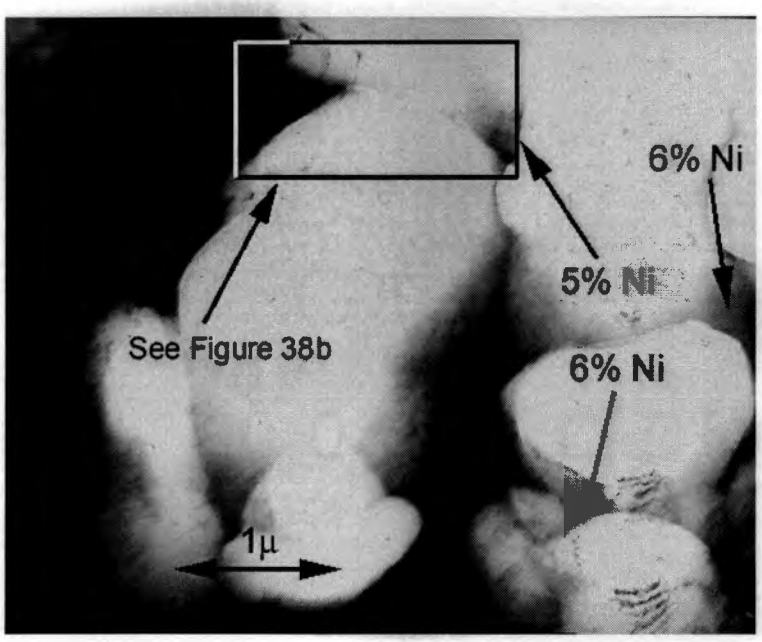


(a)

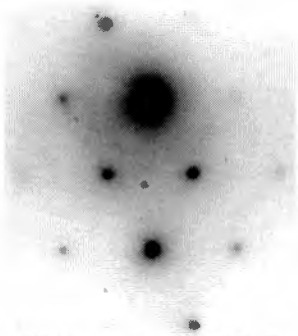
Area	%Ni
a	30
b	5
c	29
d	6
e	18
f	35
g	6
h	31
i	25
j	5

(b)

Figure 37. Microwidmanstätten α Structure in Sample D. (a) SEM image of microwidmanstätten structure in Sample D. (b) Ni content of areas notes in (a).

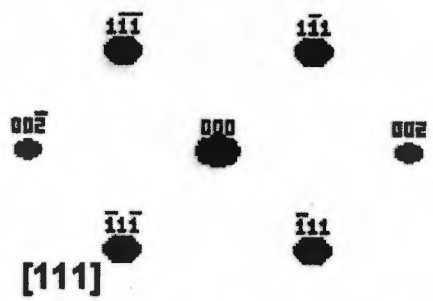


(a)



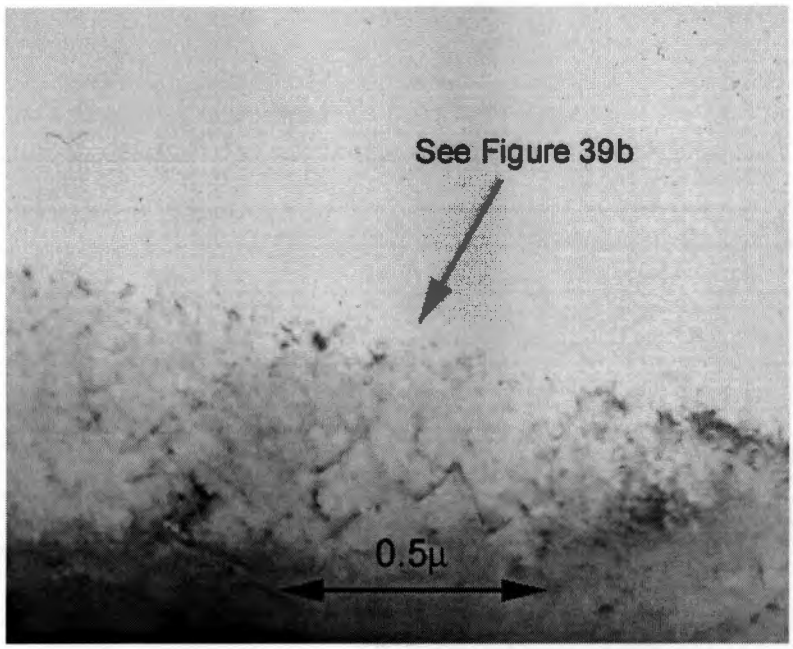
[111] a = 2.80 A

(b)

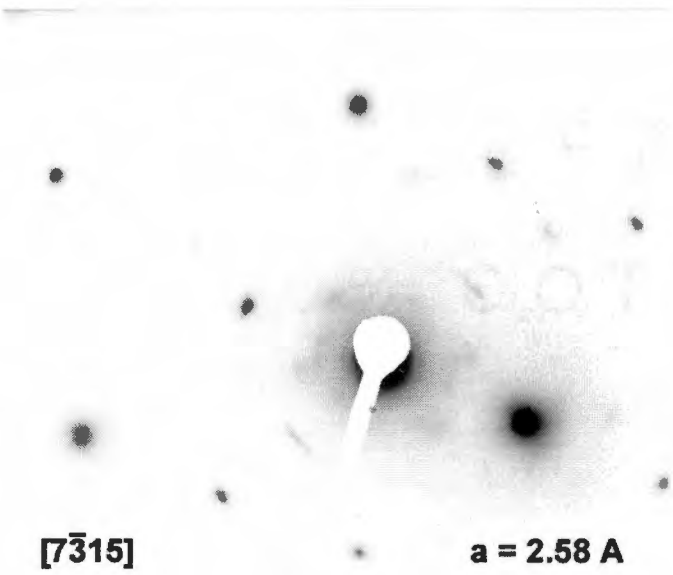


(c)

Figure 38. TEM Observation of Primary α. (a) α from Sample D. (b) SADP from noted area in (a). (c) Calculated diffraction pattern for a [111]zone axis of a bcc structure.



(a)



(b)

Figure 39. TEM Observation of Primary α. (a) TEM image of primary α from Sample D. (b) SADP from noted area in (a). Note that the zone axis was too high for the programs.

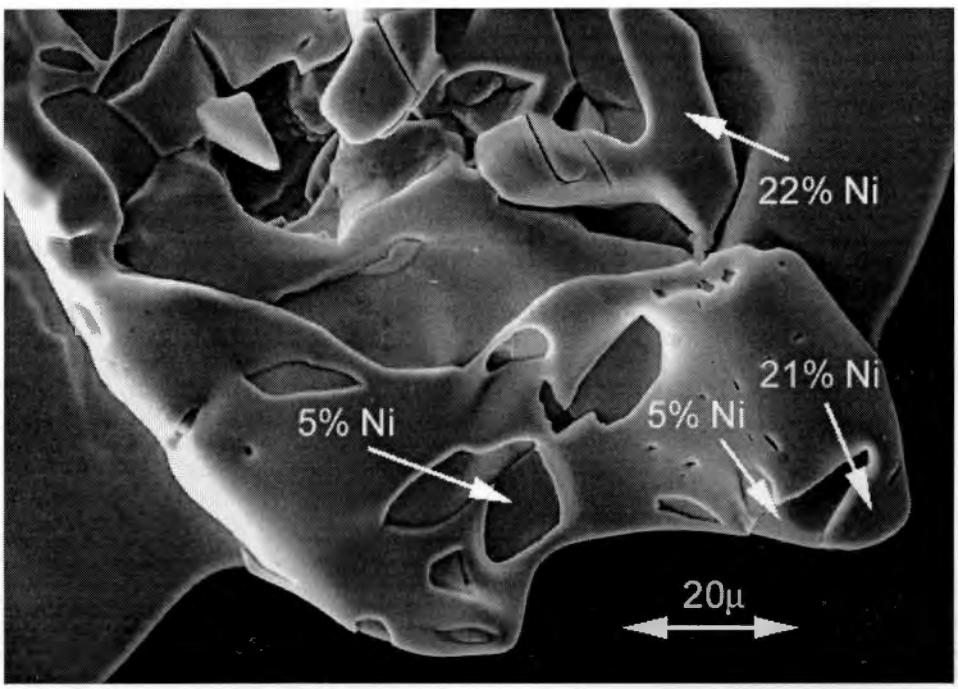


Figure 40. SEM Image of Microwidmanstätten α Structure from Sample E.

assumption can be made as to whether these regions are tetrataenite or not. At the locations assumed to be α, the Ni content was less, ~5%.

Sample F contained a stringer with a microwidmanstätten α structure and martensite, as seen in Figure 41. Martensitic structures are indicated. Each structure, both the γ and martensite, contained relatively the same Ni content, 13 to 19%. These values may also be influenced by the phase beneath the surface. At another region of Sample F, the γ region had a higher Ni content, ~23%. See Figure 42. It is not possible to determine if the high NI regions are tetrataenite. The Ni content of the α was ~<3%.

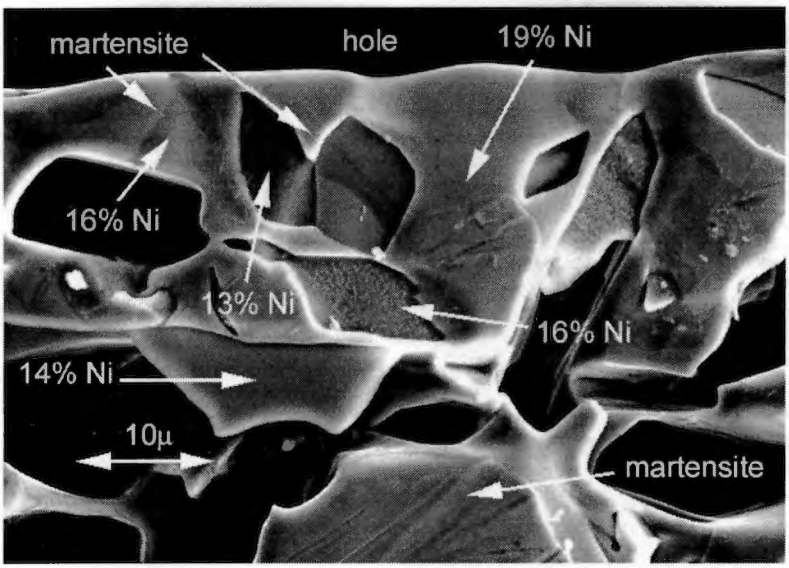


Figure 41. SEM Image of Electropolished Microwidmanstätten α Structure from Sample F.

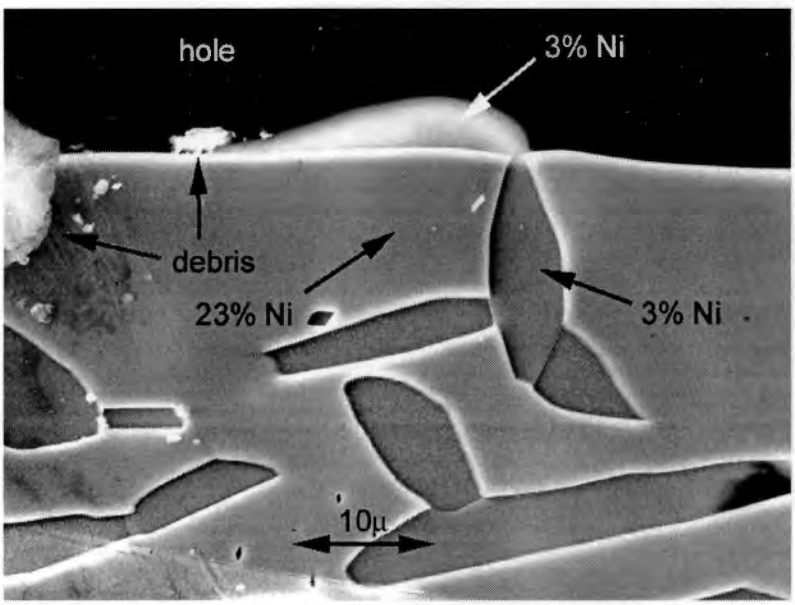


Figure 42. SEM Image of Microwidmanstätten α Structure from Sample F.

VIII. Discussion

The intent of this study was to identify the phases of the lamellar plates in pearlitic plessite and the γ spheroids in spheroiditic plessite, as well as the γ phase in the microwidmanstätten α structure. It was speculated that the high-Ni phase, γ, in the structures was tetrataenite (γ''), NiFe, an ordered fcc structure. Furthermore, the study was to investigate differences in the γ phase as the lamellar structure coarsened to coarse pearlitic plessite and to spheroiditic plessite. Several samples with pearlitic plessite and microwidmanstätten α were observed. The results of the observations are summarized in Table 4.

The criteria that should be met in order to establish the presence of tetrataenite are as follows: 1) superlattice spots observed in the SADP, 2) agreement between the calculated and observed diffraction patterns, 3) agreement with the lattice parameter of tetrataenite; 4) Ni content of about 50%. As seen in Table 4, two regions satisfy the criteria of showing superlattice spots. One of these regions had EDS analysis revealing a Ni content of the γ plate as ~50%. The other regions observed had zone axes for which the SADPs were identical for disordered γ and tetrataenite. Also the calculated lattice parameter was in agreement with the lattice parameter of γ and tetrataenite. Most of these regions had a Ni content of 40-50% Ni. Despite the lack of superlattice spots in the SADPs, these regions may be tetrataenite.

With the phases in the lamellar structure identified, an examination of how the structure formed is now presented. The formation of the retained γ stringer is described first. The dashed vertical line at approximately 8% Ni on the Fe-Ni phase diagram in Figure 43 represents the bulk Ni content of the Arispe meteorite. At Point 1, the meteor (the Arispe meteorite is still in outer space and will cool to room temperature well prior to its terrestrial life) has cooled to the γ / (γ+α) solute line, and the α begins to precipitate from the γ at ~720°C. The microstructure of the meteor prior to and at (or just below) Point 1 is shown in Figures 44a and b, respectively. Figures 45a and b show the Ni profile across these phases. Further cooling of the meteor to Point 2 in Figure 43 results in the microstructure shown in Figure 44c and the Ni profile shown in Figure 45c. Note

Table 4. Summary of TEM Observations

Sample	Phase	Figure	%Ni	Zone Axis	Superlattice Spots
A	γ	18	-	[110]	Y
A	γ	18	-	[101]	N
A	α	19	6	[100]	-
A	α	19	7	[100]	-
A	γ	21	-	[013]	N
A	γ	22	-	[101]	N
A	γ	24	50	[111]	N
A	α	24	7	-	-
A	γ	25	50	[101]	N
A	γ	26	50	-	-
A	α	26	5	-	-
A	γ	28	48	[110]	Y
A	γ	29	42	[011]	N
A	γ	30	33	[101]	N
A	γ	31	47	[101]	N
B	γ	32	47	[156]	N
C	γ	33, 34	22, 29 44, 45	[123]	N
C	α	33, 34	6	[110]	-
C	γ	35	27, 43	[123]	N
C	α	35	5	-	-
C	γ	36	44	[123]	N
C	α	36	4 –5	-	-
D	γ	37	Various	-	-
D	α	37	5, 6	-	-
D	α	38	5, 6	[111]	-
D	α	39	-	[73 15]	-
E	γ	40	21, 22	-	-
E	α	40	5	-	-
F	γ	41	14 – 19	-	-
F	γ	42	23	-	-
F	α	42	3	-	-

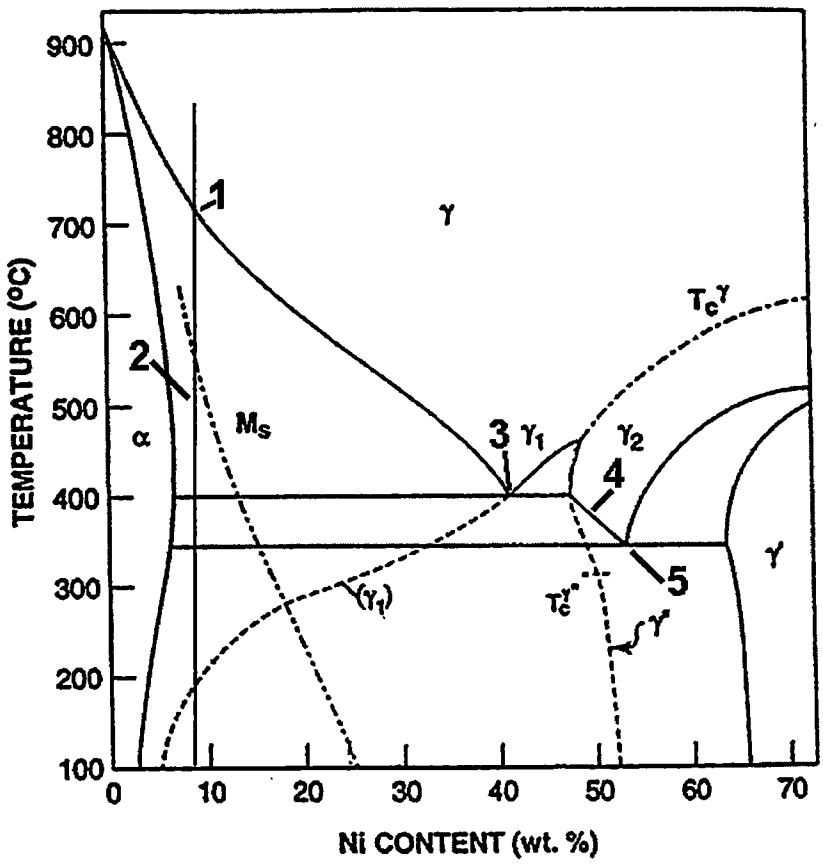


Figure 43. Fe-Ni Phase Diagram (17).

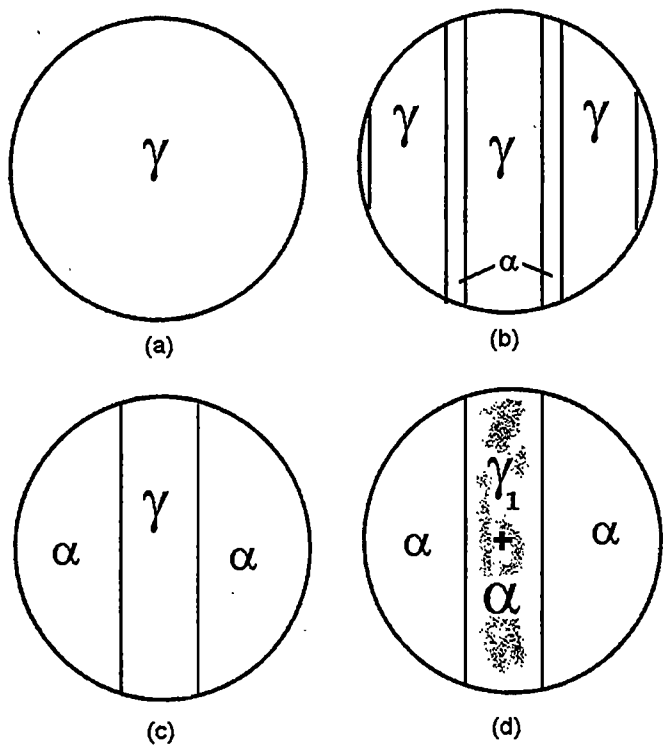


Figure 44. Schematic View of Plessite Microstructure Formation.

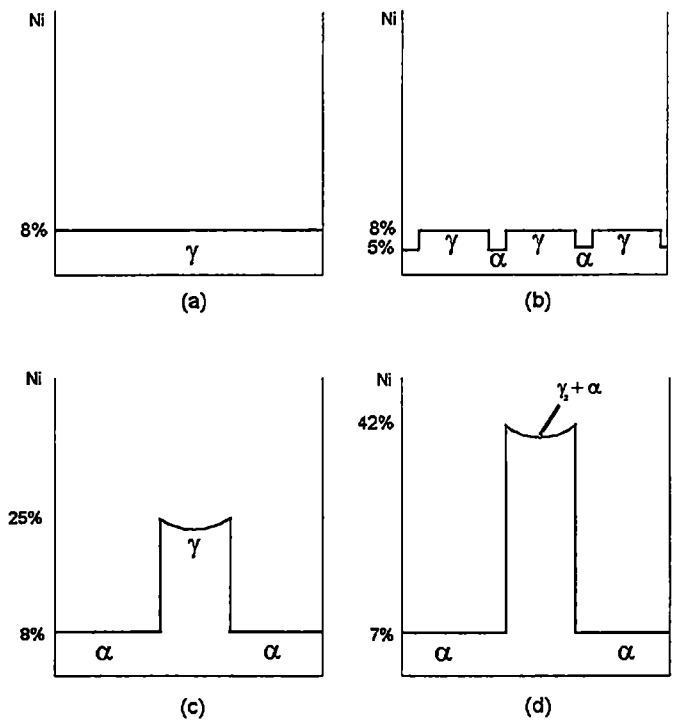


Figure 45. The M-profile Formation of the Arispe Meteorite.

the high Ni at the edges of the γ grain due to the sluggish diffusion of Ni at low temperatures. The meteor continues to cool to the monotectoid temperature, ~400°C (Point #3). The γ, which is γ_1 at this temperature and Ni content, now undergoes the monotectoid reaction shown in Equation 1.

$$\gamma_1 (41\%Ni) \rightarrow \alpha(7\%Ni) + \gamma_2(48\%Ni) \qquad \text{(Eqn. 1)}$$

The decomposition of the γ_1 to α and γ_2 results in plessite, the α and γ_2. The primary α surrounding the γ grain reaches a Ni content of ~7%. The final microstructure and Ni profile of the γ stringer is shown in Figures 44d and 45d, respectively.

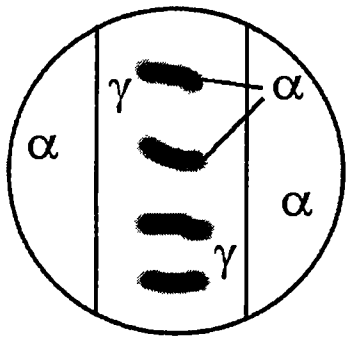
It is now assumed that the plessite resulting from the monotectiod reaction in γ_1 is the lamellar microstructure referred to as pearlitic plessite. The monotectoid reaction occurs by the α with ~8% Ni precipitating within the γ stringer and changing the Ni content of γ_1 to ~48% Ni, making it γ_2. The microstructure of the γ grain is shown in Figure 46a. Note that the α precipitates within the γ stringer and not on the stringer's boundary with the primary α. Prior to the eutectoid temperature at ~345°C (Point 4), the α has continued to precipitate within the stringer. Upon cooling from the monotectoid to the eutectoid temperature, the γ_2 increases in Ni content from ~48% Ni to ~52% Ni. The microstructure of the γ stringer prior to the eutectoid reaction is shown in Figure 46b.

The eutectoid reaction is given in Equation 2. The eutectoid reaction occurs at Point 5

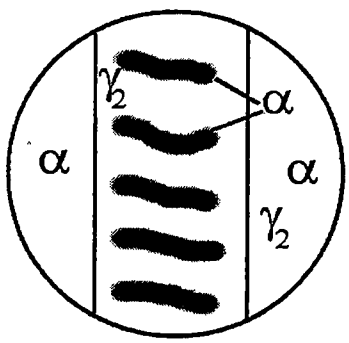
$$\gamma_2 (52\%Ni) \rightarrow \alpha(7\%Ni) + \gamma'(65\%Ni) \qquad \text{(Eqn. 2)}$$

in Figure 43. This results in the high Ni (~70%) γ'. However, a γ plate with a ~70% Ni content was never observed in the Arispe meteorite. Thus, the eutectoid reaction did not occur in the γ_2.

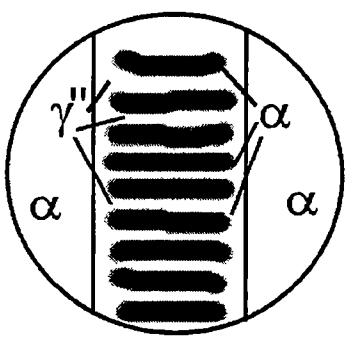
The γ_2 cools to the critical temperature, T_c, following the high Ni boundary of the spinoidal gap. At the critical temperature, the γ_2 transforms to γ", tetrataenite. The final microstructure is



(a)



(b)



(c)

Figure 46. Schematic View of Pearlitic Plessite Formation.

shown in Figure 46c. Recall that the α plates precipitated in the γ grain and not at the boundary of the γ and primary α. If a discontinuous reaction did occur, a high angle boundary must be present for the α to precipitate. A high angle boundary has not been observed in a plessite stinger. Thus the pearlitic plessite did not form by a discontinuous reaction.

As seen in Table 4, the majority of the γ plates in the microwidmanstätten α had ~30% Ni. This is significantly less than the Ni content of the γ plates in the pearlitic plessite, indicating that the microwidmanstätten α structure formed by a different mechanism than the pearlitic plessite. The formation of the microwidmanstätten α structure can be described as follows. The meteor cooled such that some of the γ with 8% Ni content transformed to γ (8% Ni) and martensite with 8% Ni. The microstructures of the γ stringer prior to the cooling is shown in Figure 47a and after forming martensite in Figure 47b.. During reheating of the martensitic plessite, the Ni diffused from the martensite to the γ and the martensite was transformed to α. The final microstructure obtained is shown in Figure 47c. It is not clear why the γ plates did not transform to γ" but remained at a ~30% Ni content.

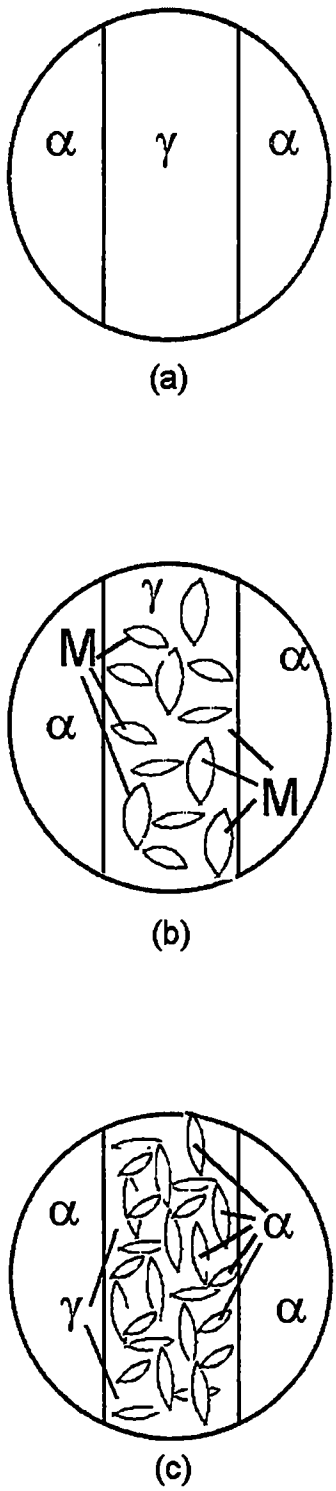


Figure 47. Schematic View of Microwidmanstättten Structure.

IX. Conclusions and Recommendations

Conclusions

1. Tetrataenite is present in pearlitic plessite.

2. Pearlitic plessite forms by a monotectoid reaction.

3. γ plates in pearlitic plessite transformed to tetrataenite after the formation of the pearlitic structure.

Recommendations

1. Determine the structure of the γ phase of the spheroids in spheroiditic plessite.

2. Determine the structure of the γ plates in microwidmanstätten α structure.

3. Identify the γ plates in coarsened pearlitic plessite.

4. Detailed determination of the M-profile of pearlitic plessite and the microwidmanstätten α structure in the Arispe iron meteorite.

REFERENCES

References

1. Mason, B., *Meteorites*, John Wiley and Sons, New York, (1962).

2. Mason, B,. Meteorites. Am. Sci. 55, p.429-455, (1967).

3. Buchwald, V. F., *Handbook of Iron Meteorites Vol. 1*, University of California Press, Berkeley, (1975).

4. Wasson, J. T., *Meteorites,* Springer-Verlag, New York, (1974).

5. Massalski, T. B., Park, F. R., Vassamillet, L. F., "Speculations About Plessite," *Geochimica et Cosmochimica Acta,* Vol. 30 (1966), p. 649-662.

6. Goldberg, E., Uchiyama, A., Brown, H., "The Distribution of Nickel, Cobalt, Gallium, Palladium, and Gold in Iron Meteorites", *Geochimica et Cosmochimica Acta,* Vol. 2 (1951), p. 1-25.

7. Lowering, J. F., Nichiporuk, W., Chodos, A., Brown, H., "The Distribution of Gallium, Germanium, Cobalt, Chromium, and Copper in Iron and Stony-Iron Meteorites in Relation to Nickel Content and Structure." *Geochimica et Cosmochimica Acta,* Vol. 11 (1957), p. 263-278.

8. Wasson, J. T., Kimberlin, J., "The Chemical Classification of Iron Meteorites. II. Irons and Pallasites with Germanium Concentrations between 8 and 100 ppm." *Geochimica et Cosmochimica Acta,* Vol. 31 (1967), p. 2065-2093.

9. Goldstein, J. I., Short, J. M., "The Iron Meteorites, Their Thermal History and Parent Bodies,"*Geochimica et Cosmochimica Acta,* Vol. 31 (1967), p. 1733-1770.

10. Dodd, R. T., *Meteorites: A Petrologic-Chemical Synthesis,* Cambridge University Press, New York, (1981).

11. McSween, Jr., H. Y., *Meteorites and Their Parent Bodies,* Cambridge University Press, New York (1987).

12. Wetherill, G. W., "An Alternative Model for the Formation of the Asteroids," *Icarus*, Vol. 100, (1992), p.307-325.

13. Yang, C. W., Williams, D. B., Goldstein, J. J., "Low-temperature Phase Decomposition in Metal from Iron, Stony-iron, and Stony Meteorites," *Geochimica et Cosmochimica Acta,* Vol. 61 (1997), p. 2943-2956.

14. Chuang, Y., Chang, Y. A., Schmid, R., Lin, J., "Magnetic Contributions to the Thermodynamic Functions of Alloys and the Phase Equilibria of the Fe-Ni System below 1200K," *Metallurgical Transactions A,* Vol. 17A, (1986), p. 1361-1372.

15. Reuter, K. B., Williams, D. B., Goldstein, J. I., "Determination of the Fe-Ni Phase Diagram below 400°C," *Metallurgical Transactions A,* Vol. 20A, (1989), p. 719-725.

16. Swartzendruber, L. J., Itkin, V. P., Alcock, C. B., "The Fe-Ni (Iron-Nickel) System," *Journal of Phase Equilibria*, Vol. 12 No. 3, (1991), p. 288-312.

17. Yang, C. W., Williams, D. B., Goldstein, J. I., "A Revision of the Fe-Ni Phase Diagram at Low Temperatures (<400°C)," *Journal of Phase Equilibria*, Vol. 17 No. 6, (1996), p. 522-531.

18. Doan, A. S., Goldstein, J. I., "The Formation of Phosphides in Iron Meteorites," *Meteorite Research,* Springer-Verlag (1969), p. 763-779.

19. Wasson, J. T., "An Equation for the Determination of Iron Meteorite Cooling Rate," *Meteoritics,* Vol. 6, (1971), p. 139-147.

20. Yang, C. W., Williams, D. B., Goldstein, J. I., "A New Empirical Cooling Rate Indicator for Meteorites Based on the Size of the Cloudy Zone of the Metallic Phases," *Meteoritics and Planetary Science,* Vol. 32, (1997), p. 423-429.

21. Buchwald, V. F., *Handbook of Iron Meteorites Vol. 2*, University of California Press, Berkeley, (1975).

22. DeMint, A.., Brooks, C. R., "Some Preliminary Metallographic Observations of the Arispe Meteorite," (M. F. Louthan, I. LeMay, G. F. Vander Voort, eds.) *Microstructural Science,* Vol. 14, ASM and IMS, Metals Park, OH, (1987), p. 239-258.

23. Cook, J. A., "Evidence for the Existence of Ordered Phases in the Plessite Stringers of the Arispe Iron Meteorite using the Transmission Electron Microscope," Unpublished research, (1994).

24. Brooks, C. R., DeMint, A.., "Some Microstructural Observations of the Pearlitic and Spheroiditic Plessite in the Arispe Meteorite," (M.E. Blum, P.M. French, R.M. Middleton, G. F. Vander Voort, eds.) *Microstructural Science,* Vol. 15, ASM and IMS, Metals Park, OH, (1988), p. 405-423.

25. Jago, R. A., "Plessite Formation and Morphology in Ataxites and Plessitic Octahedrites," *Geochimica et Cosmochimica Acta,* Vol. 45 (1981), p. 1835-1845.

26. Lin, L. S., Goldstein, J. L., Williams, D. B., "Analytical Electron Microscopy Study of the Plessite Structure in the Carlton Iron Meteorite," *Geochimica et Cosmochimica Acta,* Vol. 41 (1977), p. 1861-1874.

27. Albertsen, J. F., Jensen, G. B., Knudsen, J. M., "On the Superstructure in Meteoritical Taenite," *Meteoritics,* Vol. 13, (1978), p. 379-383.

28. Lin, L. S., Goldstein, J. L., Williams, D. B., "Analytical Electron Microscopy Study of the Plessite Structure in Four IIIC Iron Meteorites," *Geochimica et Cosmochimica Acta,* Vol. 43 (1979), p. 725-737.

29. Scott, E. R. D., Clarke, Jr., R. S., "Identification of Clear Taenite in Meteorites as Ordered FeNi," *Nature*, Vol. 281, (1979), p. 360-362.

30. Albertsen, J. F., Neilsen, H. P., Buchwald, V.F., "On the Fine Structure of Meteoritical Taenite/Tetrataenite and its Interpretation," *Physica Scripta,* Vol. 27, (1983), p. 314-320.

31. Reuter, K. B., Williams, D. B., Goldstein, J. I., "Low Temperature Phase Transformations in the Metallic Phases of Iron and Stony-iron Meteorites," *Geochimica et Cosmochimica Acta,* Vol. 52 (1988), p. 617-626.

32. Yang, C. W., Goldstein, J. I., "Phase Decomposition of Invar Alloy - Information from the Study of Meteorites," (J. Wittenauer ed.) *The Invar Effect: A Centennial Symposium,* The Minerals, Metals, and Materials Society, (1997), p. 137-146.

33. Brooks, C. R., DeMint, A., "Microwidmanstätten Ferrite and Martensite in the Arispe Iron Meteorite," (Kenny, P. J., Cole, G. S., Northwood, P. O., Wylie, J., Vander Voort, G.F., eds.), *Microstructural Science,* Vol. 17, ASM International, Materials Park, Ohio (1989), p. 471-490.

34. Kowalik, J. A., Williams, D. B., Goldstein, J. I., "Formation of the Lamellar Structure in Group IA and Group IIID Iron Meteorites," (Ruder, G. ed.), *Proceedings of the Eighteenth Lunar and Planetary Science Conference*, Cambridge University Press, New York, (1988), p. 493-501.

35. Brooks, C. R., Perrin, R., "Microstructural Observations and Mechanisms of Lamellar Coarsening in Iron Meteorites," *Microstructural Characterization,* Vol. 35, ASM International, Materials Park, Ohio (1995) p. 229-243.

36. Livingston, J. D., Cahn, J. W., "Discontinuous Coarsening in Aligned Eutectoids," *Acta Metal. 22,* (1974), p.495-503.

37. Owen, E. A., Sully, A. H., "On the Migration of Atoms in Iron-Nickel Alloys," *Phil. Mag. Vol. 31, 7th Series,* (1941), p. 320.

38. Villars, P., Calvert, L. D., *Pearson's Handbook of Crystallographic Data for Intermetallic Phases, Volume 3,* American Society for Metals International, (1991) p.2203.

VITA

Stephen Fitch was born in Worcester, Massachusetts on November 14, 1968. He attended the public school system in Lancaster, Massachusetts and graduated from Nashoba Regional High School in June, 1986. He entered The University of Tennessee, Knoxville in September, 1986. He graduated with a Bachelor of Science in Physics in December, 1990 and was commissioned in the U.S. Army Reserves as a Second Lieutenant. After graduating from the Ordnance Corps' Officer Basic Course, Stephen was employed as a laboratory technician. From July, 1993 to March, 1995, he was employed as Metallurgical Laboratory Technician at TRW, Inc. in Lebanon, Tennessee. In March, 1995 Stephen began working at Technology for Energy Corporation as a Material Test Technician. In September, he entered the Master's program in Metallurgical Engineering at The University of Tennessee, Knoxville. In May, 1997 he married Jennifer Allen. He received his M.S. in Metallurgical Engineering in December of 1999. Stephen currently resides in Knoxville, Tennessee with his wife and their two sons, Franklin and Jack.